International Journal of Fatigue 198 (2025) 109026

Contents lists available at ScienceDirect

International Journal of Fatigue

journal homepage: www.elsevier.com/locate/ijfatigue

An experimental and numerical investigation into tensile fatigue failure of composite laminates containing wrinkles and cut plies

Bing Zhang [a,b], Hafiz Ali [a], Giuliano Allegri [a], Stephen R. Hallett [a,*]

[a] Bristol Composites Institute, University of Bristol, Queen's Building, University Walk, Bristol BS8 1TR, UK
[b] Institute of Design, Robotics and Manufacturing, School of Mechanical Engineering, University of Leeds, LS2 9JT, UK

ARTICLE INFO

Keywords:
Composites
Defects
Experimental data
Fatigue modelling
Tensile loading

ABSTRACT

Fibre-reinforced polymer composites are generally seen as more fatigue resistant than metals. However, layup features such as discontinuous plies and/or manufacturing-induced defects such as wrinkles, can initiate fatigue damage and reduce the overall performance of composites. Through an extensive experimental programme and an advanced progressive damage model, this paper investigates the influence of defects and features, both in isolation and in combination, on the tensile static and fatigue performance of quasi-isotropic IM7/8552 laminates. The numerical model describes delamination and intralaminar matrix cracking using cohesive elements that follow a mixed-mode static and fatigue formulation. Experiments and modelling correlate well regarding both the ultimate static strength and S-N curves. The ultimate static strength shows a clear decreasing trend in the order of pristine, wrinkle, cut-ply and combined cut-ply & wrinkle. The cut-ply and wrinkle plus cut-ply show a similar influence on the fatigue life; both are more detrimental than wrinkle. The decrease of the fatigue life due to the defects/features can be up to two decades at a loading level corresponding to half of the pristine ultimate strength. This study implies that, for the IM7/8552 material, a wrinkle in a region of terminating plies does not add significant reduction to fatigue life.

1. Introduction

In addition to high specific stiffness and strength, another fact that drives the increasing application of Fibre Reinforced Polymer (FRP) composites in various industries is their excellent mechanical performance under cyclic loading. Nevertheless, defects are almost unavoidably induced during the manufacturing processes of composites. The manufacturing-induced defects can initiate damage due to stress concentrations and significantly degrade fatigue performance [1,2]. Typically, wrinkle defects can be induced in the consolidation process of composite components that change the ply shape or dimensions in one or multiple directions, e.g. thick laminates or curved laminates [3]. In addition, laminate features such as termination of plies/tapes are required for thickness tapering in hand lay-up or automated fibre placement (AFP) manufacture. It was shown in [4] that a cut ply, without the change in thickness, can adequately represent this feature, without the additional manufacturing complexity of thickness change. In this paper, a cut ply is classified as a feature, not a defect, since it is unavoidable and intentionally introduced in composite layups. Voids may also degrade the fatigue performance of composites [5,6], but they are not considered in this study.

In the literature, there are a limited number of studies regarding the influence of wrinkles and terminated plies on the fatigue response of composites. To control the wrinkle severity, many fatigue wrinkle studies introduce fibre waviness into an otherwise conventional laminate panel by inserts, which must however provide only a minor contribution to the stiffness of the specimen in the loading direction. Hörrmann et al. [7] successfully introduced out-of-plane wrinkle into a unidirectional laminate by inserting two 0.5 mm diameter polymer rods transverse to the fibre direction. The distance between the two rods was adjusted to control the waviness severity in the region between them. Fully reversed fatigue experiments ($R = -1$) showed that the endurance limit (at 2×10^6 cycles) was reduced by almost half when the waviness angle reached around 8.5°. Apart from wrinkle, the resin pockets due to the presence of the rods also contributed to the fatigue life reduction. Adams et al. [8] employed a three-step fabrication approach to introduce out-of-plane wrinkles into a thermoplastic laminate, namely: 1) preformation and consolidation of wavy plies; 2) insertion of thin prepreg strips and consolidation; and 3) addition of remaining plies and consolidation to form the full laminate. When the maximum wrinkle

* Corresponding author.
E-mail address: stephen.hallett@bristol.ac.uk (S.R. Hallett).

https://doi.org/10.1016/j.ijfatigue.2025.109026
Received 28 January 2025; Received in revised form 10 April 2025; Accepted 23 April 2025
Available online 26 April 2025

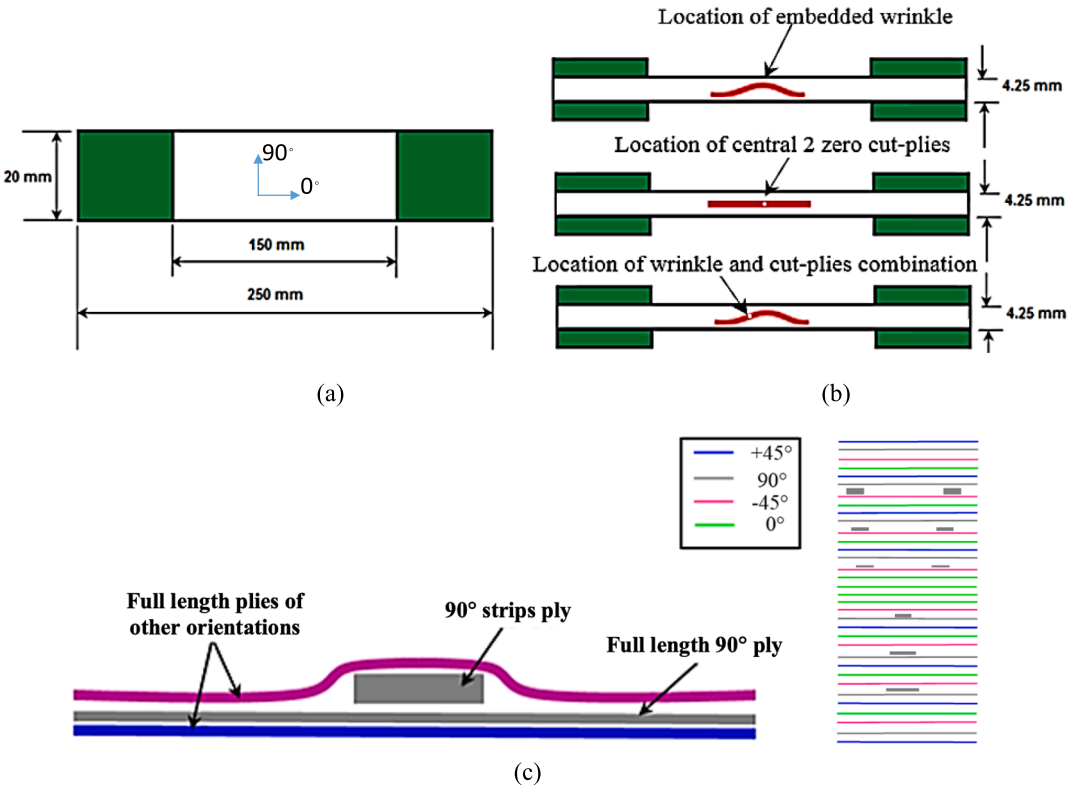

Fig. 1. (a) In-plane dimensions of the IM7/8552 composite specimens tested in this study, (b) illustration of the three defect/feature types considered in this study, and (c) illustration of the locations where 90° narrow strips were inserted during lay-up to create the out-of-plane wrinkle defect.

angle reached 5.7°, the compressive fatigue life ($R = 10$) was decreased by 1.5 decades in comparison with a pristine specimen. Mendonça et al [9] also introduced out-of-plane wrinkle to composites by adding pre-shaped wavy plies into the lay-up sequence, They confirmed that the fatigue performance of composites decreased with the wrinkle severity through tension–compression fatigue experiments (R = −1). Mukhopadhyay et al. [10] experimentally demonstrated the detrimental effect of out-of-plane wrinkles on the tensile fatigue life ($R = 0.1$) of a quasi-isotropic FRP laminate, where wrinkle was induced by inserting narrow pre-preg strips at multiple locations throughout the thickness. The introduced wrinkle had the maximum fibre waviness angle at 7.5°, and it reduced the tensile fatigue life by approximately an order compared to a pristine specimen. Wang et al. [11] successfully introduced wrinkles into continuous plies by placing two blocks of dropped plies anti–symmetrically on each side of the continuous plies. Compressive fatigue ($R = 10$) tests showed that the specimen failed mainly due to delamination between the dropped plies and the wavy continuous plies. Miao et al [12] introduced wrinkles to a full-scale wind turbine blade by adding cured epoxy inserts in the lay-up sequence, along with three debonding defects. Post-fatigue analysis showed that the fracture of the wrinkled sections is dominated by Mode-II delamination. More recently, they investigated the influence of wrinkles on the compression-compression (R = 10) fatigue performance of carbon/glass hybrid composite laminates using the same wrinkle-introducing approach [13]. They found that debonding between resin inserts and adjacent plies occurred first, followed by interlaminar cracks. Differently, when Spencer and Chen [14] studied the tensile fatigue (R = 0.1) performance of a wrinkled hybrid laminate, interlaminar cracks occurred earlier than the debonding between resin inserts and adjacent plies.

Regarding the influence of a cut ply, Elsherbini et al. [15] experimentally evaluated the tensile fatigue ($R = 0.1$) performance of a carbon/epoxy laminate with an 'enclosed' ply cut, which did not extend to the laminate edges. The degradation of the laminate fatigue life due to the ply cut increased with the applied stress in comparison with pristine specimens, and the reduction could reach three decades when the laminate had a cross-ply stacking sequence. Elsherbini et al. [15] believed that there was a threshold stress value below which the delamination initiating from the enclosed ply-cut stopped propagation after a number of cycles. On the other hand, when considering a 'through-width' cut inside a laminate, Wisnom et al. [4] and Allegri et al [16] did not find clear evidence of a load threshold below which delamination growth would not happen, even down to the delamination growth rate in the order of 10^{-8} mm/cycle that was considered by Allegri et al [16].

Fatigue progressive damage models (FPDM) are very helpful for examining the detailed failure mechanisms of composites containing defects, and can significantly save experimental costs. Nevertheless, a limited number of studies are available in this area. Nikishkov et al. [17] built a ply-by-ply model for predicting the fatigue life of a wrinkle laminate, with each interlaminar interface described by a layer of solid elements. The FPDM used by Nikishkov et al. [17] combined stress-based failure criteria (Hashin and LaRC criteria), S-N curves and a linear cumulative damage rule for damage initiation. A sudden stiffness degradation approach was used to simulate material response after damage initiation. Elsherbini [18] extended the FPDM developed by Shokrieh [19] to study the fatigue effect of the 'enclosed' ply-cut mentioned before. Elsherbini [18] used a gradual degradation approach to decrease the stiffnesses and strengths of elements with the number of cycles until damage was detected by stress-based failure criteria. After damage onset a sudden degradation approach was adopted to exclude failed elements from carrying load. Apart from experiments, Mukhopadhyay et al. [10] also presented a ply-by-ply FPDM with cohesive elements inserted between and within plies to simultaneously predict the onset and growth of delamination and intralaminar matrix cracking, respectively. The cohesive elements in this case followed a fatigue bilinear cohesive law, whereby the cohesive strength of an element was degraded according to an S-N curve for fatigue damage initiation. The fatigue propagation stage was described by reducing the

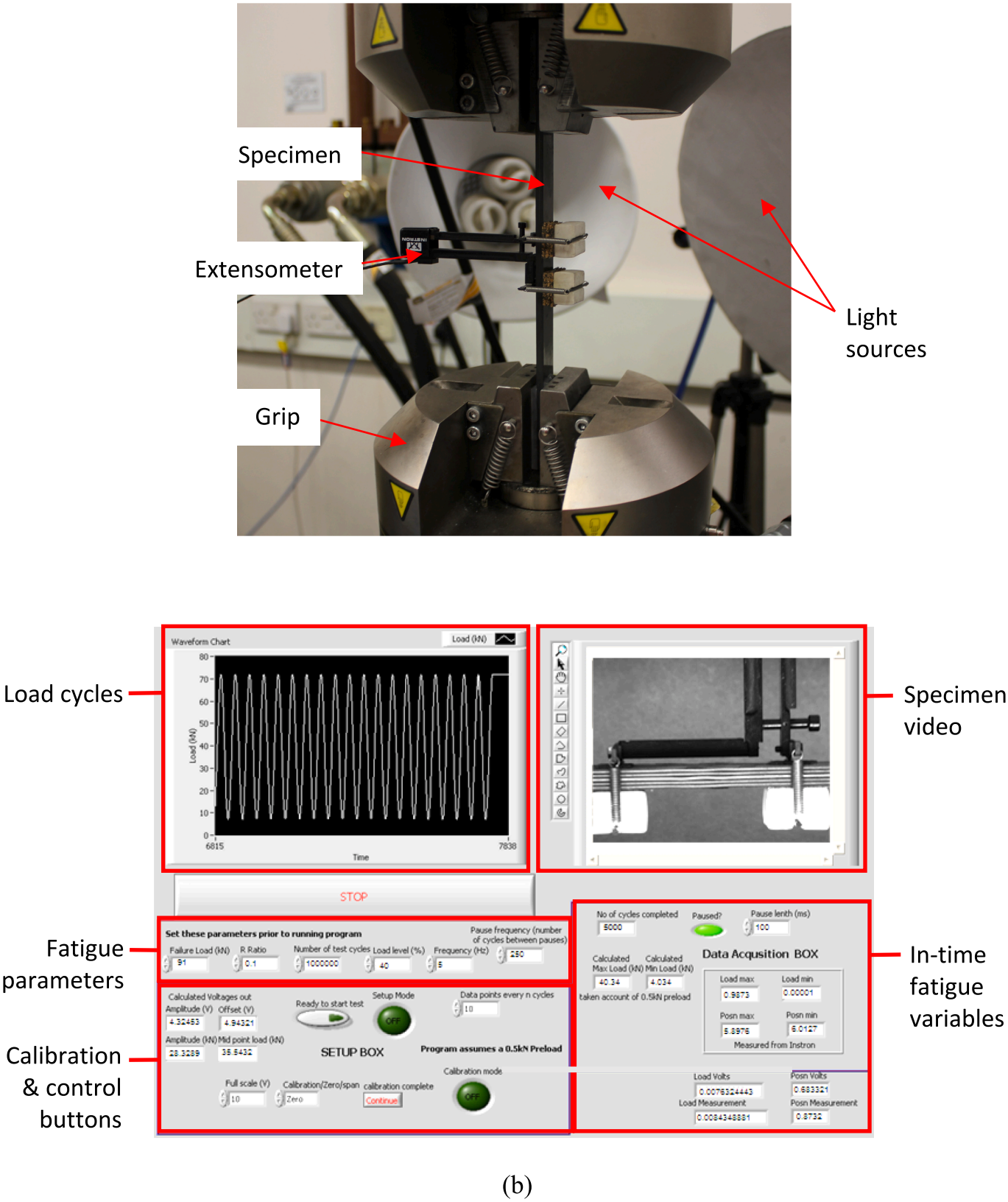

Fig. 2. (a) Experimental set–up for fatigue tests, and (b) graphical user interface in the NI/LabVIEW programme for fatigue tests.

cohesive stiffness according to a variant of the Paris law for fatigue damage propagation.

It can be concluded that the literature regarding the influence of wrinkles and cut plies on the tensile fatigue behaviour of composite laminates is quite sparse. Systematic investigations regarding the combination of wrinkles and cut plies are completely lacking. This study aims to fill this knowledge gap by using extensive experiments and advanced numerical modelling, investigating in detail the effects of

three defect and feature cases, i.e. out-of-plane wrinkle, cut ply and combined wrinkle & cut ply, on the tensile fatigue performance of composites. As has been demonstrated in the literature [20,21], the integrity of composite structures is influenced locally by manufacturing-induced defects or features. This supports the necessity of conducting such extensive studies. The main novelty of this study resides in the types of defects/features considered, especially the combined wrinkle & cut ply.

Section 2 presents the experimental programme, including specimen preparation and test set-up. A FPDM strategy is presented in Section 3 to simulate the fatigue failure mechanisms occurring in the specimens. Section 4 presents experimental observations and numerical simulations regarding the tensile static and fatigue behaviours of the laminates.

2. Experimental programme

2.1. Specimen manufacturing

Four types of specimens were manufactured: pristine, out-of-plane wrinkle, cut ply and combined wrinkle & cut-ply (W&C). The specimens were made of IM7/8552 prepreg (Hexcel, UK) following a quasi–isotropic stacking sequence, i.e. $[(45^\circ/90^\circ/\text{-}45^\circ/0^\circ)_4,0^\circ]_s$. As shown in Fig. 1a, the specimens had a length of 250 mm and a width of 20 mm. 50 mm long cross-ply glass FRP tabs were attached to both ends of the specimens, giving a gauge length of 150 mm. As shown in Fig. 1b, the specimens had a total thickness of 4.25 mm, with each continuous ply being 0.125 mm thick after cure.

For manufacturing these specimens, a laminate panel was first manually laid up for each specimen type in a clean room. During lay-up, a debulking procedure by vacuum bagging at room temperature was performed after every fourth ply for the pristine panel and the cut-ply panel. The debulking procedure was performed after every two plies for the wrinkle and W&C panels. Defects were seeded into these panels during the lay-up process. The wrinkle was created by inserting narrow thin 90° ply strips adjacent to the full-length 90° plies at given locations throughout the thickness of the panel, as illustrated in Fig. 1c. A similar procedure was used in Ref. [10]. In the top half of the wrinkle panel, the inserted 90° strips gradually increased in the number of plies from the centre onwards (1, 2 and 3 plies, with a nominal thickness of 0.125 mm, 0.25 mm and 0.375 mm, respectively), but had the same width (3 mm). In the bottom sub-laminate, the inserted strips gradually increased in width (3, 4 to 5 mm), but all had the same number of plies (2 plies, with a nominal thickness of 0.25 mm). During the natural process of wrinkle formation, neat resin tends to fill the gap around the wavy fibres, but this mechanism is difficult to reproduce when artificially inducing wrinkles. In place of neat resin, the 90° strips used here are completely orthogonal to the loading direction and their behaviour is resin-dominated, thus their effect on the overall load–displacement response is expected to be negligible [10]. This method also avoids the introduction of any pre-cured or 'foreign' material into the laminate, or the creation of additional interfaces since the added strips merge with adjacent 90° plies, thus minimising the chance of delamination from the wrinkle-inducing strips.

To introduce the cut-ply feature, the two middle 0° plies were first vacuum consolidated and then cut at the gauge-section centreline. The cut plies were then added to the laminate stack. For the panel with the combined wrinkle and cut, the manufacturing procedure to introduce out-of-plane waviness was the same as for the wrinkle-only case. However, contrary to the cut-ply only panel, the ply termination was introduced at 2 mm offset from the gauge-section centreline, to introduce the cut as close as possible to the maximum wrinkle angle.

The laminate panels were vacuum bagged and cured in an autoclave following the manufacturer's recommendations (2 h at 180 °C at 7 bar pressure). The cured panels were trimmed using a water-cooled diamond saw, making sure that the defects were positioned at the centre of the panels. End tabs were attached to these panels using an epoxy adhesive (Araldite 2015). All surfaces to be bonded were grit blasted and degreased prior to bonding, to achieve optimum strength. Finally, the panels were carefully cut into individual specimens.

2.2. Experimental set-up

2.2.1. Quasi-static test

To study the influence of defects on tensile strength and provide reference loads for the fatigue characterisation, quasi-static tests were performed prior to fatigue tests. The quasi-static specimens were loaded at 0.5 mm/min under displacement control. The coupons were carefully aligned within the machine grips before loading. The 'pristine' specimens were tested in a calibrated Instron 1342 servo–hydraulic machine equipped with a 250 kN load cell. The 'defect' specimens were tested in a calibrated Instron 8801 servo-hydraulic machine equipped with a 100 kN load cell. Load and crosshead displacement were continuously recorded via the test machine computerised control systems. To capture the onset and propagation of damage, a high-speed camera was focussed on the specimen gauge section. Two high-power light sources were used to illuminate the specimens during tests.

2.2.2. Fatigue test

Tension-tension cyclic tests were conducted with an R ratio of 0.1. Fatigue peak loads were defined referring to the ultimate tensile strengths achieved in the quasi-static tests. Three fatigue severities were considered for each type of specimens, specifically 70 %, 50 % and 40 % for the pristine case, and 60 %, 50 % and 40 % for the defect cases, relative to their respective static ultimate strengths. As shown in Fig. 2a, a clip-gauge extensometer with a span of 25 mm was attached to the specimen gauge section to record the effective tensile strain. In combination with an FPGA card, an NI/LabVIEW® programme was built to control the loading machine, record the tensile strain data from the extensometer and control a CCD camera that was focused on the specimen gauge section. As shown in Fig. 2b, to execute any given test, the operator simply needs to input the relevant fatigue parameters via a graphic interface, specifying the quasi-static reference strength, specimen dimension, loading severity, R ratio, fatigue frequency and the final number of cycles. The programme provides a sinusoidal load signal for the fatigue loading. The fatigue frequency was adjusted to keep the loading rate consistent throughout all the cases, specifically, 3.5 Hz, 4 Hz and 5 Hz respectively for the 60 %, 50 % and 40 % severities, and 3 Hz for the 70 % severity in the pristine case. The frequencies used here, between 3.5 Hz and 5 Hz, are intended to be low enough that there is no effect of loading frequency [22–24], but the strategy of keeping loading rate constant ensures this. The programme halted the machine at the peak load for 0.5 s after a prescribed number of cycles and triggered the CCD camera to take photos under constant load. The fatigue tests were run on an Instron 8801 servo-hydraulic machine.

3. Numerical modelling

This section describes the progressive damage finite element (FE) models that were built to analyse the tensile static and fatigue performance of the composite specimens. The numerical simulations were carried out using the commercial FE software Abaqus/Explicit 2018.

3.1. Mesh generation

The procedure followed to create the FE meshes is described below.

1) A layer of single integration-point (IP) hexahedral elements (C3D8R element in Abaqus) was used to describe each ply. To reduce computational cost, only the middle 90 mm length of the laminates' gauge section was included in the ply-level mesh. The ply-level mesh consisted of a 30 mm-long fine mesh region in the middle, and the mesh density gradually decreased from the fine mesh region towards

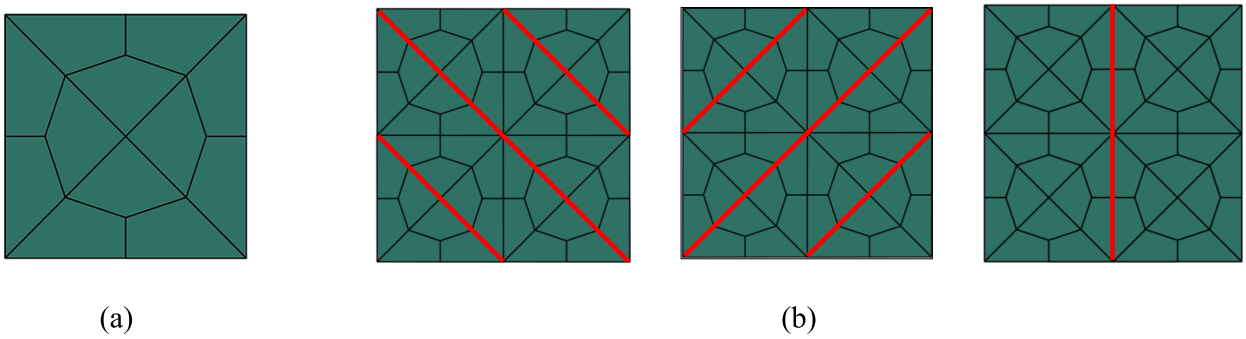

Fig. 3. (a) In-plane view of the unit-cell mesh, and (b) illustration of the cohesive elements (in red) inserted within or between the unit cells for predicting intralaminar matrix cracking, respectively in −45° plies, +45° plies and 90° plies from left to right.

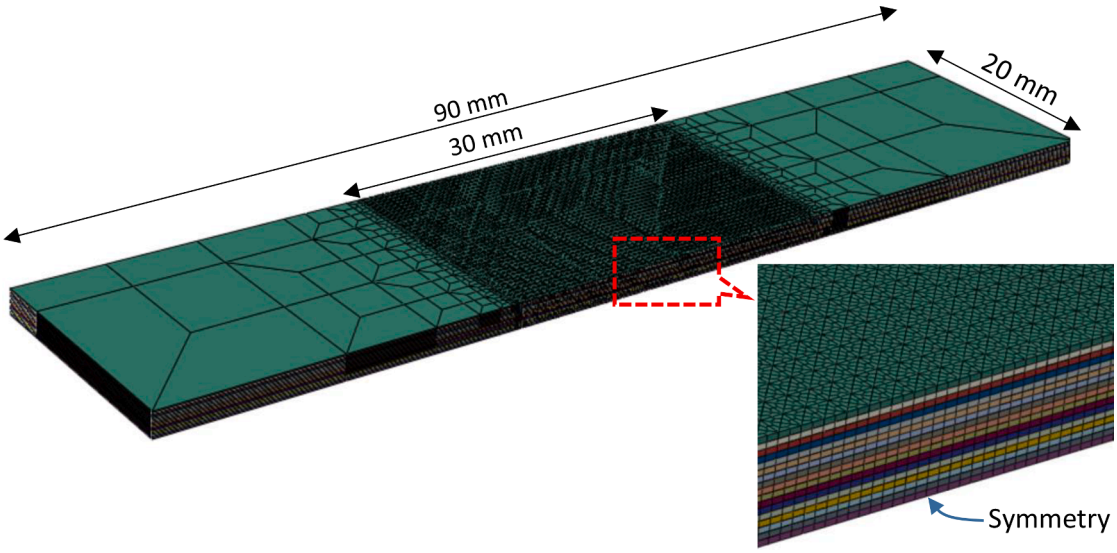

Fig. 4. Snapshot of the pristine laminate model.

the ends of the ply-level mesh. The fine mesh region was generated by repeating a unit-cell mesh along the length and width directions of the ply. As shown in Fig. 3a, the unit cell has equal in-plane sides (0.5 mm), with thickness equal to that of IM7/8552 plies (0.125 mm).

2) 34 layers of the ply-level mesh were then stacked to create the full thicknesses of the wrinkle model and the W&C model. The pristine and cut-ply specimens are symmetric relative to their mid planes, thus only half of their thicknesses were modelled, with appropriate symmetry boundary condition.
3) 1×10^{-3} mm thick and four-IP cohesive elements (COH3D8 element in Abaqus) were inserted between adjacent plies for predicting delamination. The generated interlaminar interfaces had the same in-plane mesh as their neighbouring plies. Thus, they were connected via shared nodes, which avoid any time-consuming constraint definition.
4) 1×10^{-3} mm thick and four-IP cohesive elements were also inserted along the fibre-orienting diagonals of the unit cells in −45° plies for predicting matrix cacking, as shown in Fig. 3b. Similarly, cohesive elements were inserted along the relevant diagonals of the unit cells in + 45° plies and between two adjacent unit cells in 90° plies for the matrix cracking prediction. Matrix cracking is assumed not to occur in the 0° plies. Inserting cohesive elements within a ply mesh simply required splitting each node along the insertion path into two nodes to accommodate the cohesive element thickness. The pristine laminate mesh can be achieved up to this step and is shown in Fig. 4.
5) The cut-ply feature was represented by removing a row of unit-cell meshes from the middle of the 0° cut ply, as shown in Fig. 5. To create the wrinkle defect, the well-polished side of a pre-test wrinkle specimen was microscopically scanned, as shown in Fig. 6a. The centre-lines of all 0° plies were then extracted based on the different grey level of 0° plies compared to angled plies. The coordinates of all

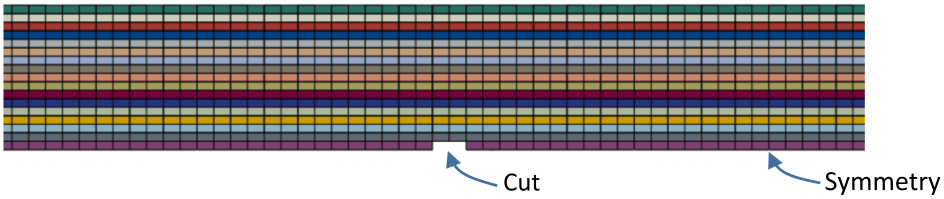

Fig. 5. Side view of the cut-ply model.

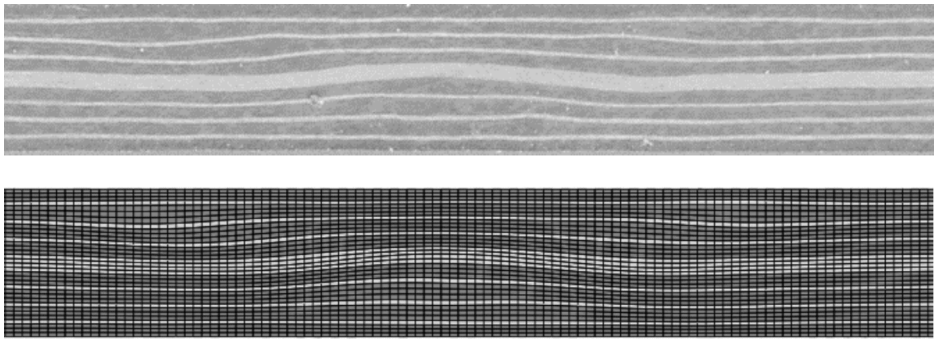

Fig. 6. Microscopic scan (top) and numerical description (bottom) of the wrinkle laminate (0° plies in light grey, angle plies in dark grey).

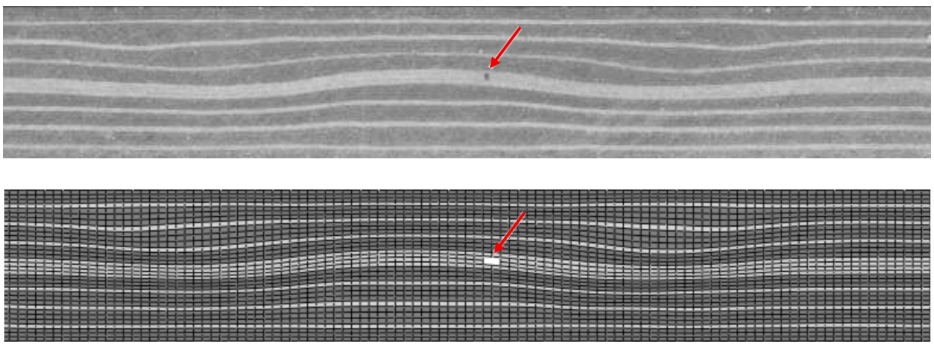

Fig. 7. Microscopic scan (top) and numerical description (bottom) of the combined wrinkle & cut-ply laminate (0° plies in light grey, angle plies in dark grey); cut locations are indicated by red arrows.

Table 1
Ply material properties and cohesive properties used in this study.

Ply properties [10,25–28]		Interface properties [10,25,27,28,41]	
E_{11}(MPa)	161,000	G_{IC}(N/mm)	0.2
$E_{22} = E_{33}$(MPa)	11,380	G_{IIC}(N/mm)	1.0
$G_{12} = G_{13}$(MPa)	5170	σ_I^{max}(MPa)	60
G_{23}(MPa)	3980	σ_{II}^{max}(MPa)	90
$\nu_{12} = \nu_{13}$	0.32	K_I(N/mm^3)	1.0×10^5
ν_{23}	0.436	K_{II}(N/mm^3)	1.0×10^5
$\alpha_{22} = \alpha_{33}$(℃$^{-1}$)	3.0×10^5	η	0.3
α_{11}(℃$^{-1}$)	0		
Paris law parameters by Allegri's approach [27,45]			
C(mm/cycle)	3.51×10^{-2}	b	14.05
h	1.457		
Fatigue initiation parameters [10,26,43]			
a_I	0.072	a_{II}	0.071

the element nodes in the model thickness direction were adjusted referring to the 0° ply centre-lines extracted from the microscopy scans. As compared in Fig. 6a and b, the wrinkle model can accurately capture fibre waviness throughout the laminate. The central four 0° plies feature the most severe waviness. The maximum wrinkle angle was measured by the tangent of the top surface of the central wavy 0° plies relative to the laminate length direction. The maximum wrinkle angle is 5.2° on average, which is smaller than the one (7.5°) reported in Ref. [10]. Fig. 7 shows that the W&C mesh also agrees well with the W&C specimen regarding the wrinkle feature and the ply-cut location. A row of unit-cell meshes were deleted at the ply-cut location in the W&C model. Comparing Fig. 6 and Fig. 7 shows that the W&C defect laminate has a very similar wrinkle feature to the wrinkle-only laminate, which is expected, since they used the same method to introduce wrinkles (Fig. 1c).

All the mesh generating procedures explained above were implemented in a Fortran 90 script, except for the image-based wrinkle generation algorithm, that was written in MATLAB. The meshing package was an upgraded version of the one developed in Ref. [10], mainly by incorporating the image-based wrinkle mapping algorithm and an output interface for Abaqus keywords.

3.2. Ply material properties

The material properties used for the IM7/8552 plies are given in Table 1 [10,25–28]. The material axes of the ply elements were defined using the mid-planes of the elements instead of their nodes, which allows better representation of fibre orientation (axis 1) in the wrinkle region. As the ultimate strengths were determined by catastrophic fibre failure, it was necessary to include fibre failure in the models. The fibre failure criterion introduced in [25], based on a Weibull strength distribution, was employed:

$$\sum_{i=1}^{N_E} V_i \bullet \left(\frac{\sigma_i}{\sigma_{\text{unit}}}\right)^m \geq 1 \tag{1}$$

whereby N_E is the number of ply elements in a model; V_i is the element volume; σ_i is the fibre-direction tensile stress of an element; σ_{unit} is the unidirectional failure stress of a unit volume of material; m is the Weibull modulus. σ_{unit} and m were assigned 3131 MPa and 40 in the models, derived from scaled unidirectional tensile tests on IM7/8552 [25].

3.3. Simulation steps

Both the static strength and fatigue performance of the laminates were simulated via the numerical models. All the models had a thermal step, where a −160° temperature variation field was applied to the whole models over 0.5 s, to simulate the effect of post-cure cool-down before any mechanical loading.

In the static models, mechanical loading was applied via the left and

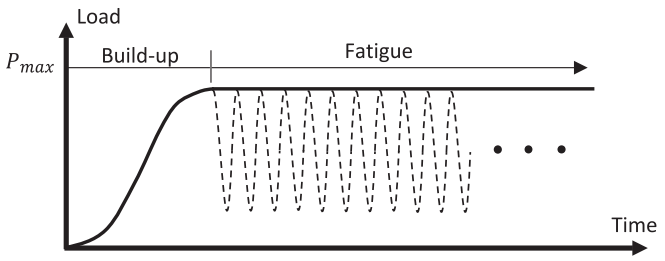

Fig. 8. Load history in the mechanical step of a fatigue model.

right surfaces under displacement control until catastrophic fibre failure occurred. On the other hand, the mechanical step in the fatigue models was defined following the single load envelope approach [26,29–38]. As shown in Fig. 8, the fatigue mechanical step comprised a build-up stage and a fatigue degradation stage. In the build-up stage, the model was loaded to the fatigue load peak (P_{max}) over one second, following a smooth function to reduce possible kinetic effects. The model then remained loaded at the peak load envelope throughout the fatigue stage, while locally the intra and interlaminar cohesive elements were degraded as a function of the number of cycles by following the fatigue cohesive formulation that will be introduced in the next section. A load-holding stage could be added between the build-up stage and the fatigue degradation stage to reduce possible kinetic effects [32]. However, the fatigue defect models run in this study showed a very small kinetic energy at the end of the build-up stage, and the load-holding stage showed negligible influence on the fatigue damage prediction.

3.4. Static & fatigue cohesive formulation

Several fatigue cohesive formulations proposed in the literature are based on a bilinear static cohesive law [10,26,27,29–32,39]. The static bilinear cohesive law proposed in Ref. [40] is used here, as shown in Fig. 9a. The static cohesive law is first described below, before the fatigue law is introduced.

3.4.1. Static cohesive law

The cohesive element used in this study has four Newton-Cotes integration points at its mid-plane corners, as shown in Fig. 9b. The cohesive law describes the deformation of an interface by 3 orthogonal displacements (opening δ_{33}; shear δ_{13} and δ_{23}) at each integration point. The 3-axis at each IP is orthogonal to the mid-plane of the cohesive element. The 1–2 plane is orthogonal to the 3-axis. The specific 1- and 2–axis directions are not critical here, as the resultant shear displacement is used to represent overall shear component, i.e. δ_{II}. Mode I (opening) δ_I, mode II (shear) δ_{II} and mixed-mode δ_m displacements are respectively defined by:

$$\delta_I = \max(0, \delta_{33}); \delta_{II} = \sqrt{{\delta_{13}}^2 + {\delta_{23}}^2}; \delta_m = \sqrt{\max(0, \delta_I)^2 + {\delta_{II}}^2} \quad (2)$$

When the interface is not damaged, it behaves elastically (see Fig. 9a), as expressed by Eq. (3), whereby σ and K indicate the interface traction and elastic stiffness, respectively.

$$\sigma_I = K_I \delta_I, \ \sigma_{II} = K_{II} \delta_{II} \quad (3)$$

Static damage initiation is determined by a stress-based quadratic criterion [40]:

$$\left(\frac{\max(0, \sigma_I)}{\sigma_I^{max}}\right)^2 + \left(\frac{\sigma_{II}}{\sigma_{II,E}^{max}}\right)^2 = 1 \quad (4)$$

whereby σ_I^{max} is mode I strength; $\sigma_{II,E}^{max}$ is the enhanced mode II strength due to through–thickness compression (TTC), as defined by:

$$\sigma_{II,E}^{max} = \sigma_{II}^{max} - \eta \bullet min(0, \sigma_I) \quad (5)$$

whereby σ_{II}^{max} is the un-enhanced mode II strength; η is the enhancement factor, which can be determined by an ad-hoc experimental set-up [41].

When damage is initiated, the interface enters the stiffness degradation (softening) stage of the bilinear law (recall Fig. 9a). The interface degradation is controlled by a static damage variable D_s, which corresponds to the damaged area to the total area of the interface [31,40]. The variable is defined by:

$$D_s = \frac{\delta_m - \delta_m^0}{\delta_m^f - \delta_m^0} \quad (6)$$

whereby δ_m^0 and δ_m^f are the mixed-mode displacements at damage initiation and full failure, respectively.

A power law criterion is used for determining full failure:

$$\left(\frac{G_I}{G_{IC}}\right)^\alpha + \left(\frac{G_{II}}{G_{IIC,E}}\right)^\alpha = 1 \quad (7)$$

whereby the power $\alpha \in [1, 2]$ is an empirical factor derived from mixed-mode interlaminar fracture tests [40]. G_I and G_{II} are separately mode I and mode II strain energy release rates (SERRs), which correspond to the integrals of traction times separation on the individual mode response curves (illustrated by dashed blue lines in Fig. 9a). G_{IC} is mode I critical

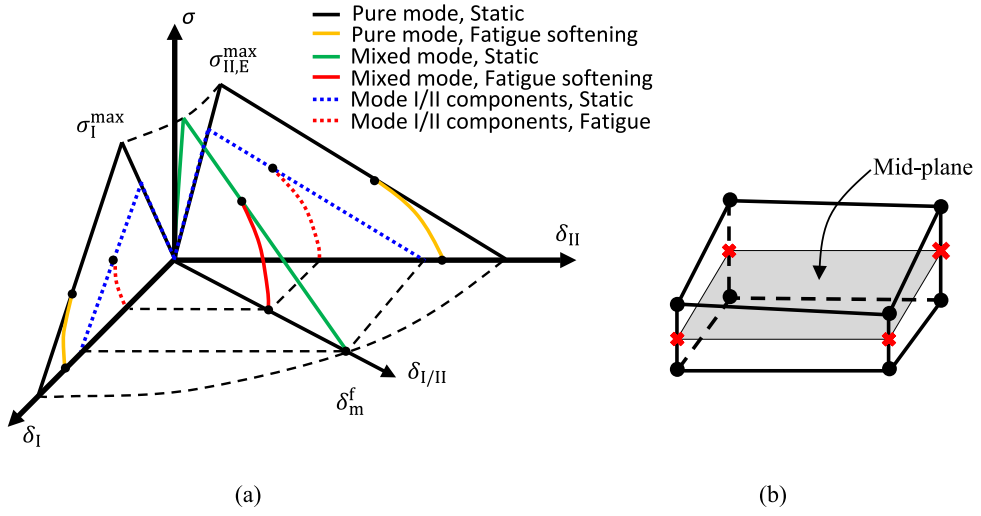

Fig. 9. (a) Mixed-mode static and fatigue cohesive law; (b) an Abaqus COH3D8 cohesive element (element nodes in block dots and integration points in red crosses).

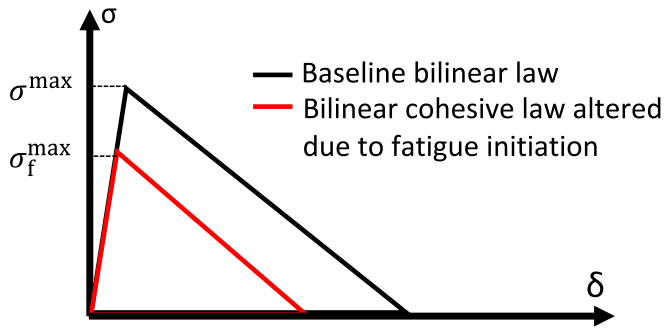

Fig. 10. Effect of fatigue initiation on the bilinear cohesive law.

SERR. $G_{IIC,E}$ is the enhanced mode II critical SERR due to through thickness compression (TTC), as defined by Eq. (8) based on the un-enhanced mode II critical SERR G_{IIC} [42].

$$G_{IIC,E} = \left(\frac{\sigma_{II,E}^{max}}{\sigma_{II}^{max}}\right)^2 G_{IIC} \tag{8}$$

Mode I and II tractions in the stiffness degradation region are determined by:

$$\sigma_I = K_I^D \delta_I, \sigma_{II} = K_{II}^D \delta_{II} \tag{9}$$

whereby the degraded stiffness pair K_I^D and K_{II}^D are determined by the static damage variable D_s by [31,40]:

$$K_I^D = (1-D_s)\frac{\delta_m^0}{\delta_m} K_I,\ K_{II}^D = (1-D_s)\frac{\delta_m^0}{\delta_m} K_{II} \tag{10}$$

3.4.2. Fatigue cohesive law

3.4.2.1. Fatigue damage initiation. For a given mode mixity, fatigue damage initiation in an IM7/8552 interface can be estimated by a linear function between the maximum stress (S) and the logarithm of the number of cycles to damage N_i [26,43,44]:

$$\frac{S}{\sigma^{max}} = 1 - a_m \bullet \log_{10} N_i \tag{11}$$

whereby σ^{max} is the static strength; The *S-N* constant a_m is here estimated assuming a simple displacement-based interaction between mode I and mode II components [26,43]:

$$a_m = a_I \bullet \left(\frac{\delta_I}{\delta_m}\right)^2 + a_{II} \bullet \left(\frac{\delta_{II}}{\delta_m}\right)^2 \tag{12}$$

whereby a_I and a_{II} are respectively the *S-N* constants for pure mode I and pure mode II, which can be measured by ad-hoc tests [44]. The loading severity, corresponding to the left-hand side of Eq. (11), is evaluated by a quadratic combination of mode I and mode II contributions:

$$\frac{S}{\sigma^{max}} = \sqrt{\left(\frac{\sigma_I}{\sigma_I^{max}}\right)^2 + \left(\frac{\sigma_{II}}{\sigma_{II,E}^{max}}\right)^2} \tag{13}$$

Combining Eq. (11), Eq. (12) and Eq. (13), the number of cycles to fatigue initiation N_i can be obtained as:

$$N_i = 10^{\frac{1-\sqrt{\left(\frac{\sigma_I}{\sigma_I^{max}}\right)^2 + \left(\frac{\sigma_{II}}{\sigma_{II}^{max}}\right)^2}}{a_I \bullet \left(\frac{\delta_I}{\delta_m}\right)^2 + a_{II} \bullet \left(\frac{\delta_{II}}{\delta_m}\right)^2}} \tag{14}$$

The *S-N* relationship in Eq. (11) describes the fatigue life under a constant stress. To consider the possible variation of cyclic stress peak during the loading history of the interface, the Palmgren-Miner linear damage rule is used by:

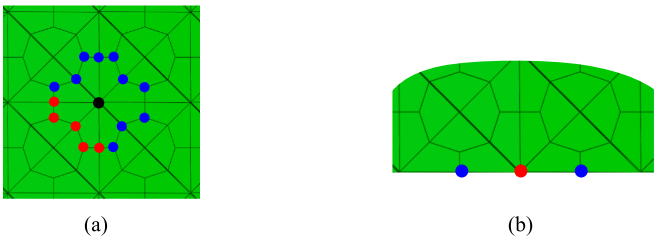

Fig. 11. Illustrations of a damaged IP becoming a crack tip (a) when at least one of its neighbouring IPs is failed or (b) when the IP is located at a model edge (black dot: failed IP; red dots: new fatigue crack-tip IPs; blue dots: elastic IPs).

$$D_i^t = D_i^{t-dt} + \frac{f_N \bullet dt}{N_i^t} \tag{15}$$

whereby D_i is the damage initiation variable; f_N is the numerical fatigue frequency, which is commonly assigned a much larger value than the frequency used in experiments to speed up simulation [27]; dt is the time increment; N_i^t is the value of N_i for the stress level at the time t, derived according to Eq. (14).

The fatigue initiation law was only applied to the integration points that are in the elastic stage of the cohesive law. When the fatigue initiation variable D_i of an IP reaches unity, the IP is forced to enter the softening region of the cohesive law by reducing the interface strength. The fracture toughness is also degraded, equaling the square of the strength reduction, as shown in Fig. 10 [10,36]. By assuming that mode I and II strengths have the same degradation ratio, the degraded strength pairs due to fatigue initiation are thus defined by Eq. (16), whereby δ_m^i is the mixed-mode displacement at fatigue initiation.

$$\sigma_{I,f}^{max} = \frac{\delta_m^i}{\delta_m^0}\sigma_I^{max};\ \sigma_{II,f}^{max} = \frac{\delta_m^i}{\delta_m^0}\sigma_{II,E}^{max} \tag{16}$$

3.4.2.2. Fatigue damage propagation. Fatigue delamination propagation rate (da/dN) depends on SERR, mode mixity and stress ratio. Allegri et al. [45] proposed to consider these factors by using a variant of Paris law, as expressed by:

$$\frac{da}{dN} = C\left(\frac{G}{G_C}\right)^{\frac{b}{(1-R_\sigma)^{1+\alpha e^{-h\varnothing}}}} \tag{17}$$

whereby a is the delamination length; G_C is the critical SERR, which can be derived from Eq. (7) for a given mode mixity. C, b and h are material-dependent parameters; The parameter α describes the interaction between stress ratio R_σ and mode mixity, and it is expressed by Eq. (18); The SERR G is the sum of G_I and G_{II}. The stress ratio R_σ is here assumed to equal the global load R ratio. The assumption works well for single load cases, such as the uni-axial tensile cases consider here [10,17,26]. When there is non-proportional loading, e.g. the combination of quasi-static loading and fatigue is considered, two twin cohesive models can be employed to estimate the local stress ratio [27,46,47].

$$\alpha = \frac{G_C - G_{IC}}{G_{IIC,E} - G_{IC}} \tag{18}$$

A fatigue cohesive zone may cover multiple elements, although it is shorter than a static cohesive zone for the same material system. Applying the fatigue propagation law to the full fatigue cohesive zone may overestimate the crack growth, as fatigue damage generally accumulates in the crack tip region, which is smaller than the total fatigue cohesive zone. Thus, Kawashita et al. [32] proposed to apply the fatigue propagation law only to the element that represents a crack tip. This method has been successfully applied in other studies [10,26,27]. The crack-tip tracking was implemented at the element level in [10,26,27,32], while it is here extended to the integration-point level.

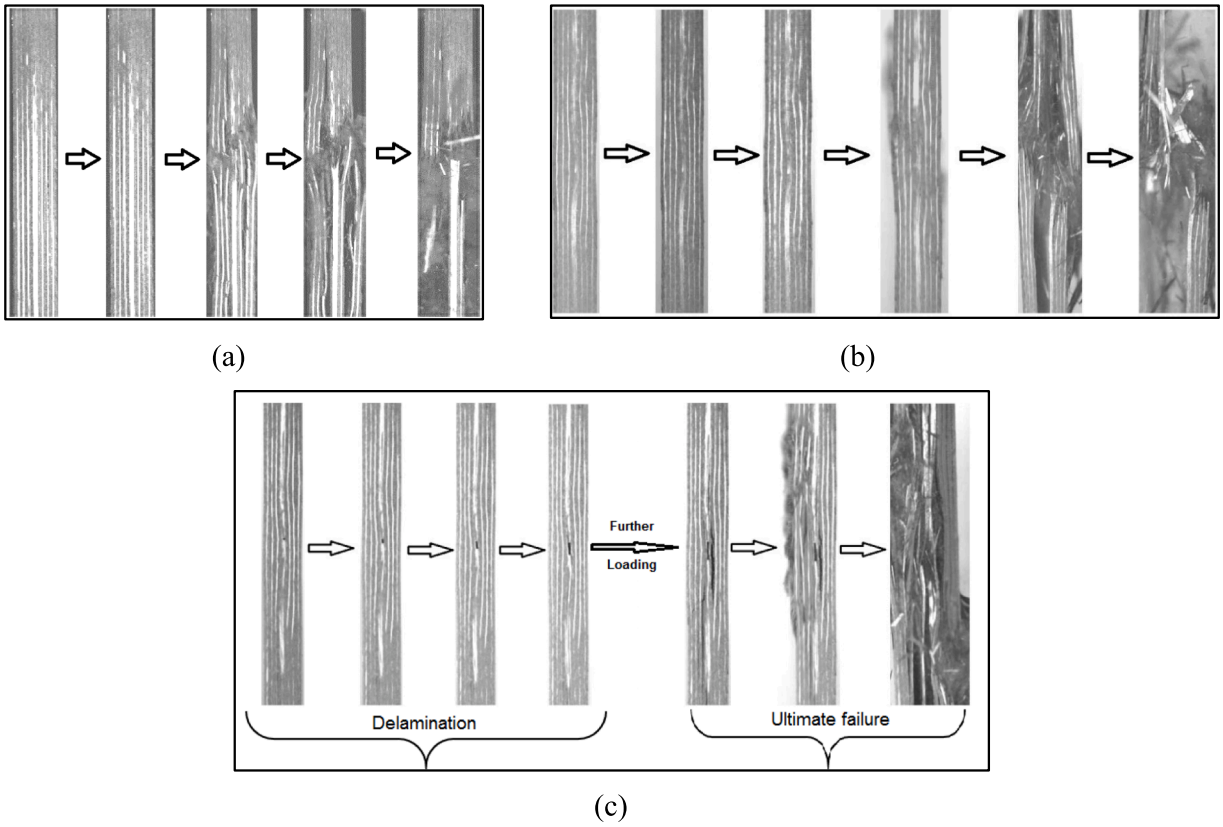

Fig. 12. Selected snapshots of (a) a pristine specimen, (b) a wrinkle specimen and (c) a W&C specimen captured at 140,000 frames per second during quasi-static tests.

Two criteria need to be met so that an IP becomes a fatigue crack tip: 1) firstly, the IP is damaged, in other words, it has entered the softening region of the static cohesive law (recall Fig. 9a); 2) at least one of its neighbouring IPs is fully failed or the IP is at a discontinuous location (e.g. an edge of a model), as shown in Fig. 11a-b on a portion of the mesh created in Section 3.1. When an IP becomes a fatigue crack tip, it enters the stiffness degradation region of the fatigue cohesive law (recall Fig. 9a). The stiffness degradation algorithm is explained below.

The number of cycles that a crack-tip IP can sustain before full failure, ΔN_e, is evaluated by:

$$\Delta N_e = \frac{\mathrm{d}N}{\mathrm{d}a} l_\mathrm{f} \tag{19}$$

whereby l_f is the fatigue characteristic length, namely, the length that a crack-tip IP represents in the crack growth direction. Here, the l_f value of a crack-tip IP is estimated as the square root of a quarter of its host element in-plane area, by assuming that each IP of a 4-IP cohesive element represents a quarter of the element volume.

When a crack-tip IP has the static damage variable D_s, it needs to accumulate additional fatigue damage equivalent to $1 - D_\mathrm{s}$ to reach full failure over the number of cycles to failure (i.e. ΔN_e as given by Eq. (19). Thus, the fatigue damage rate can be evaluated by [32]:

$$\frac{\mathrm{d}D_\mathrm{f}}{\mathrm{d}N} = \frac{1 - D_\mathrm{s}}{\Delta N_\mathrm{e}} \tag{20}$$

In an explicit FE programme, the fatigue damage variable is updated by Eq. (21) [32]. Then, the total damage variable D_t is calculated as the sum of D_s and D_f. The degraded stiffnesses of a crack-tip IP are computed by replacing D_s with D_t in Eq. (10), then the traction components are derived by Eq. (9).

$$D_\mathrm{f}^{\mathrm{t+dt}} = D_\mathrm{f}^{\mathrm{t}} + \frac{\mathrm{d}D_\mathrm{f}}{\mathrm{d}N} \bullet f_\mathrm{N} \bullet \mathrm{dt} \tag{21}$$

The fatigue cohesive formulation and the fibre failure criterion as described above were implemented via a user-defined material subroutine in Abaqus/Explicit 2018. The cohesive properties used here for the IM7/8552 laminates are included in Table 1 [10,25–28,41,43,45].

4. Results and discussion

4.1. Quasi-static

In the initial tests, pristine specimens consistently failed at the edge of end tabs, possibly due to the stress concentration developed in the 'step down' transition regions from tabs to the gauge section. To overcome this issue, three 300 mm long pristine specimens were manufactured without end tabs and directly clamped at a 75 mm length on both sides. The pristine specimens without end tabs failed in the gauge section due to fibre failure, as shown in Fig. 12a. The pristine specimens had a mean ultimate strength at 1071.7 MPa with a 2.89 % coefficient of variation (CV).

All defect specimens were tested using end tabs and were found to fail in the gauge section. 4 wrinkle specimens were tested and only 2 showed very small load drops before final failure. Fig. 12b presents the selected snapshots of a wrinkle specimen from elastic deformation to catastrophic failure. The mean ultimate strength of the wrinkle specimens was 899.9 MPa with a 3.37 % CV. Three cut-ply specimens were tested; all showed a clear load drop before final failure. This corresponded to the onset of delamination between the two cut plies and their adjacent continuous plies, and the corresponding stress level is thus denoted as delamination strength. The mean delamination strength of the cut-ply specimens was 637.6 MPa with a 3.71 % CV, and the mean

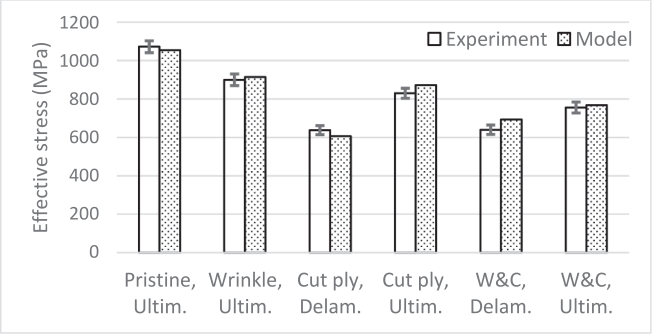

Fig. 13. Comparison between measured and predicted quasi-static strengths.

ultimate strength was 830 MPa, with a 3.13 % CV. Three tested W&C specimens also showed apparent delamination between the cut plies and continuous plies before final fibre failure. Fig. 12c presents the selected snapshots of a W&C specimen from elastic deformation to catastrophic failure. The mean W&C delamination strength was 639.8 MPa with a 3.81 % CV, and the mean ultimate strength was 755.7 MPa with a 3.79 % CV.

As shown in Fig. 13, the numerical models give good predictions of the quasi-static strengths for all these laminates. The differences between numerical models and experimental averages are −1.73 %, 1.63 %, −5.00 %, 5.16 %, 8.42 % and 1.63 %, respectively, for the pristine ultimate strength, the wrinkle ultimate strength, the cut-ply delamination strength, the cut-ply ultimate strength, the W&C delamination strength, and the W&C ultimate strength. The maximum difference is observed in the W&C delamination strength, but it remains less than 10 %. When comparing all the static cases, the ultimate strength shows a clear decreasing trend in the order of pristine, wrinkle, cut-ply and W&C. The coupons where wrinkles and cut plies co-existed suffered a larger reduction in the ultimate strength than the specimens where single or no defects/features were introduced. It is also interesting to notice that the W&C delamination strength is close to the cut-ply

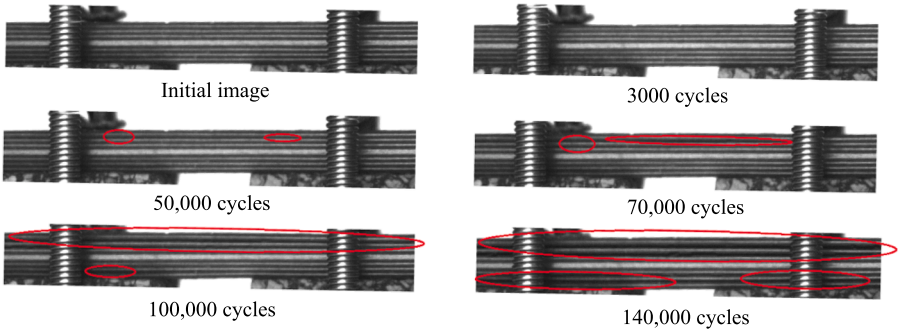

Fig. 14. Camera images from side view of an IM7/8552 pristine specimen loaded at 50% severity showing delamination growth (highlighted in red circles) at various stages of fatigue cycling.

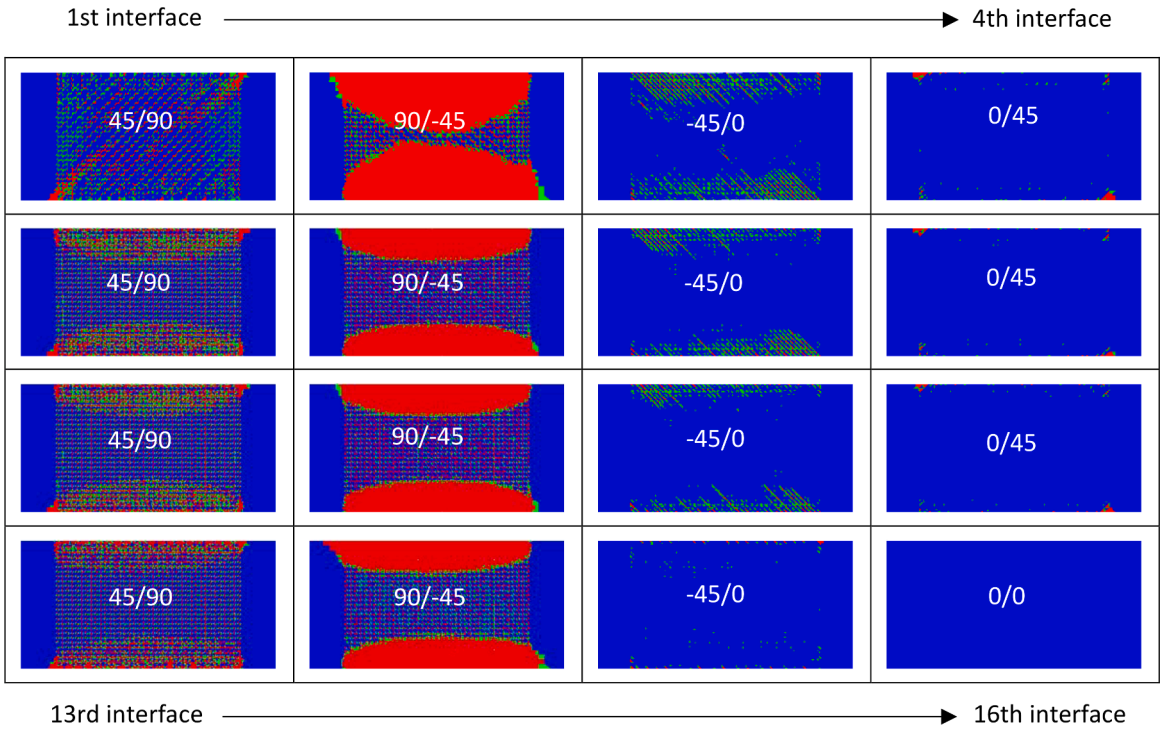

Fig. 15. Top view of the predicted interlaminar failure for the pristine 50% severity case at 50,000 cycles; note that half laminate was modelled due to symmetry (red: full failure; green: damaged; blue: elastic).

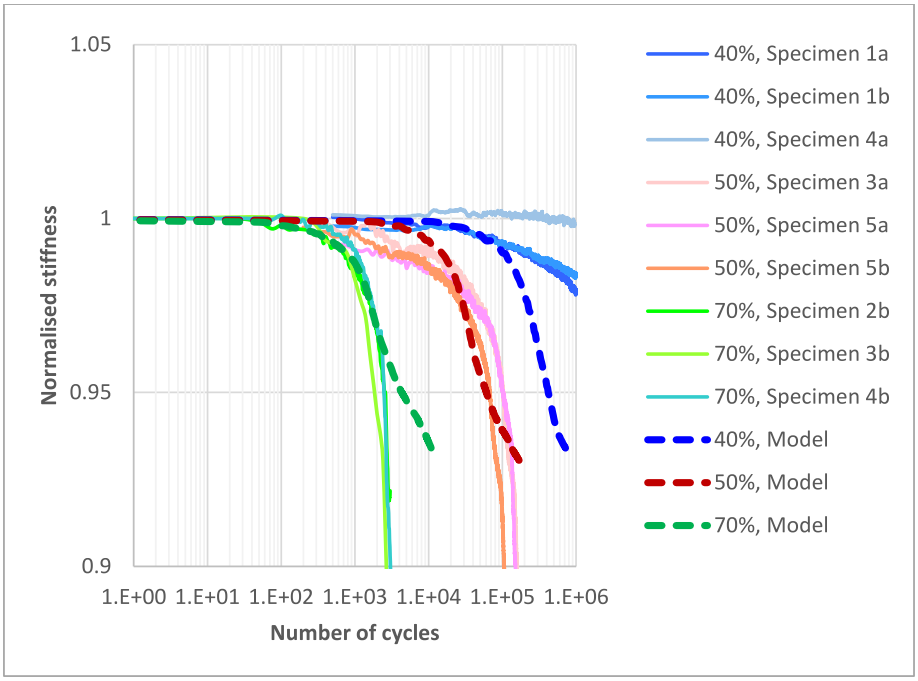

Fig. 16. Experimental measurements and model predictions regarding the normalised stiffness versus number of cycles of the "pristine" laminates.

delamination strength.

The maximum difference between prediction and measurement regarding the ultimate strength appears in the cut-ply case (5.16 %). This is potentially because that, different from other cases, the cut-ply laminate was dominated by the delamination emanating from central cuts and along the interfaces between the two central cut 0° plies and their adjacent continuous 0° plies. When the interlaminar crack entered the coarse mesh regions on both sides of the model (recall Fig. 4), the interlaminar strength and toughness were artificially increased [48]. This caused a delay of fibre breakage in the middle fine mesh region, and thus an increase of the ultimate strength. Although other cases share the same mesh configuration with the cut-ply case, the influence from the coarse mesh regions is less significant, due to the extensive damage occurring in the middle fine-mesh region. Thus, for the cut-ply case, it makes more sense to select the delamination strength as the baseline for fatigue modelling, as such strength is not affected by the coarse mesh region. Severities of 40 %, 50 % and 60 % relative to the ultimate strength of the cut-ply case correspond to the severities of 52 %, 65 % and 78 % in terms of its delamination strength; these were used for the cut-ply fatigue modelling.

4.2. Fatigue

4.2.1. Pristine

In the pristine experimental case, delamination onset and damage growth occurred mainly at the 90°/±45° interfaces, as observed in Fig. 14. FE modelling revealed that the 90°/-45° interfaces showed more severe delamination than the 45°/90° interfaces at any given number of cycles, and the 90°/-45° delamination is more severe closer to the laminate surface, as shown in Fig. 15. The interlaminar failure initiated from the specimen edges and progressed inwards with cyclic loading, driven by free edge stress concentrations. This description of interlaminar failure is consistent across all the three severities for pristine coupons. Extensive intralaminar matrix damage was also observed in experiments, as well as predicted in the FE models.

For a quantitative assessment, Fig. 16 plots the normalised stiffness versus number of cycles (E-N) for the pristine case. To minimise the influence of coarse mesh regions, FE results were cropped at around 5 % stiffness knock-down. Considering that fatigue tests in this study were under load control, i.e. constant minimum and maximum loads throughout tests, the normalised stiffness E_{norm} can be computed by:

$$E_{\text{norm}} = \frac{\{\Delta L_{\max} - \Delta L_{\min}\}_0}{\{\Delta L_{\max} - \Delta L_{\min}\}_N} \tag{22}$$

where $\Delta L_{\max}$ and $\Delta L_{\min}$ are the overall elongations at the maximum and minimum loads. '0' means the end of the build-up stage, i.e. the start of fatigue loading, as shown in Fig. 8, while 'N' denotes the n-th cycle. Eq. (22) was not suitable for plotting FE results since the peak-load load envelope method was used and $\Delta L_{\min}$ was not known in models. By

Fig. 17. Camera images from side view of an IM7/8552 cut-ply specimen loaded at 40% severity showing delamination growth (highlighted in red circles) at various stages of fatigue cycling.

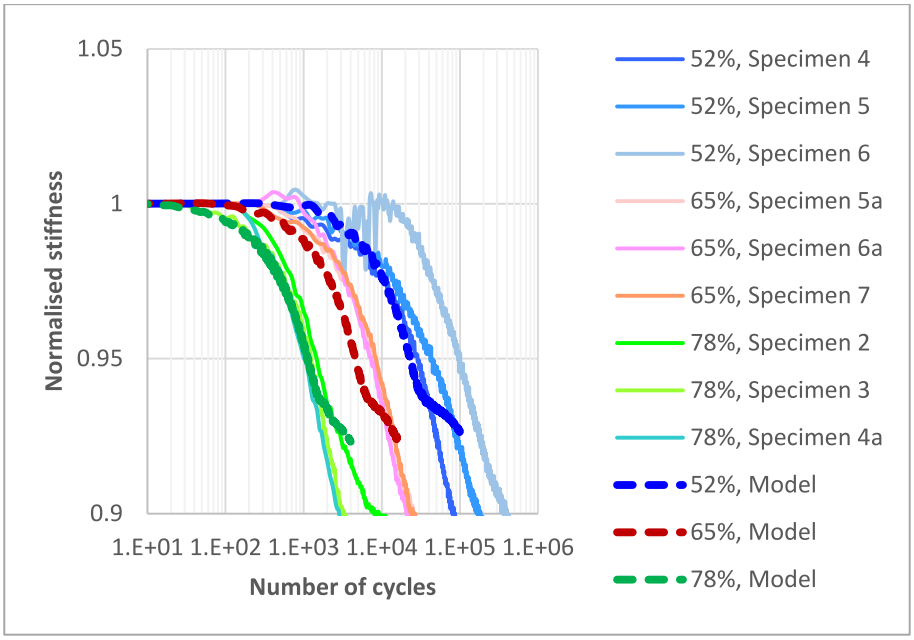

Fig. 18. Experimental measurements and model predictions regarding the normalised stiffness versus number of cycles of the "cut-ply" laminates (note: severities relative to delamination strength).

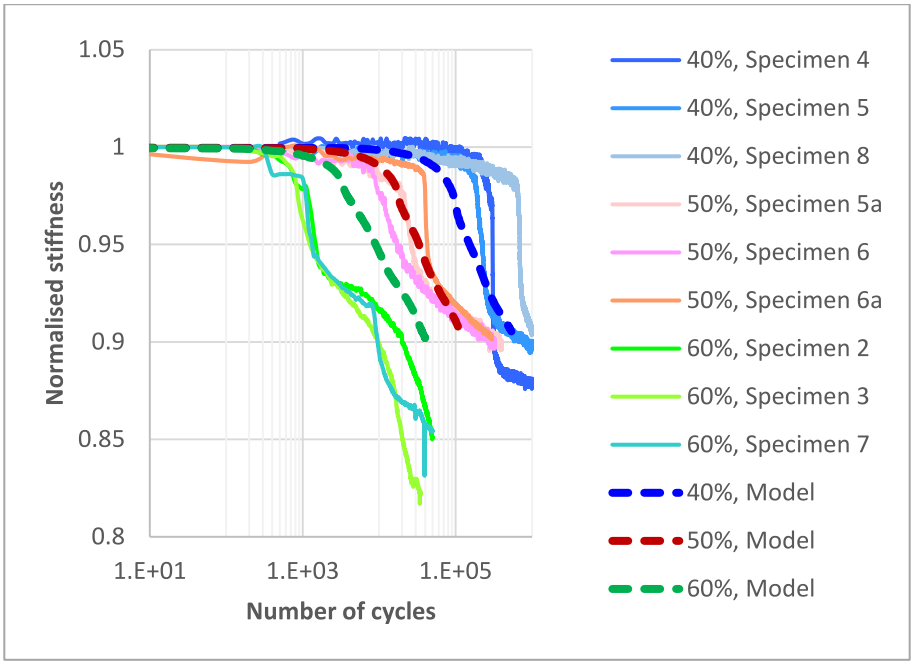

Fig. 19. Experimental measurements and model predictions regarding the normalised stiffness versus number of cycles of the "wrinkle" laminates.

assuming that $\Delta L_{\min}$ for 0.1 R ratio is negligible, Eq. (22) can be simplified to Eq. (23). To check whether the assumption is reasonable, Eq. (22) and Eq. (23) were used to plot experimental stiffness, and a negligible difference was observed between two.

$$E_{\text{norm}} = \frac{\{\Delta L_{\max}\}_0}{\{\Delta L_{\max}\}_N} \tag{23}$$

It can be seen from Fig. 16 shows that FE models correlate very well with experimental measurements in terms of E-N at the two high severities. The FE modelling predicts a greater reduction in stiffness than the experimental measurement for the 40 % severity level, indicating a conservative estimate for design purposes.

4.2.2. Cut-ply

For all fatigue severities of the cut-ply case, the stiffness decreased gradually with the number of cycles. As explained above, these fatigue severities are based on the quasi-static delamination strength, instead of the ultimate strength. The stiffness drop was associated with delamination emanating from the cut-ply defect and propagating along the interfaces between the two central cut 0° plies and their adjacent continuous 0° plies. Camera images also show that the gap between ply terminations grew with the number of cycles, as observed in Fig. 17. The normalised stiffness as a function of elapsed cycles for the cut-ply specimens is shown in Fig. 18. FE predictions agree very well with experimental measurement for all the three severities.

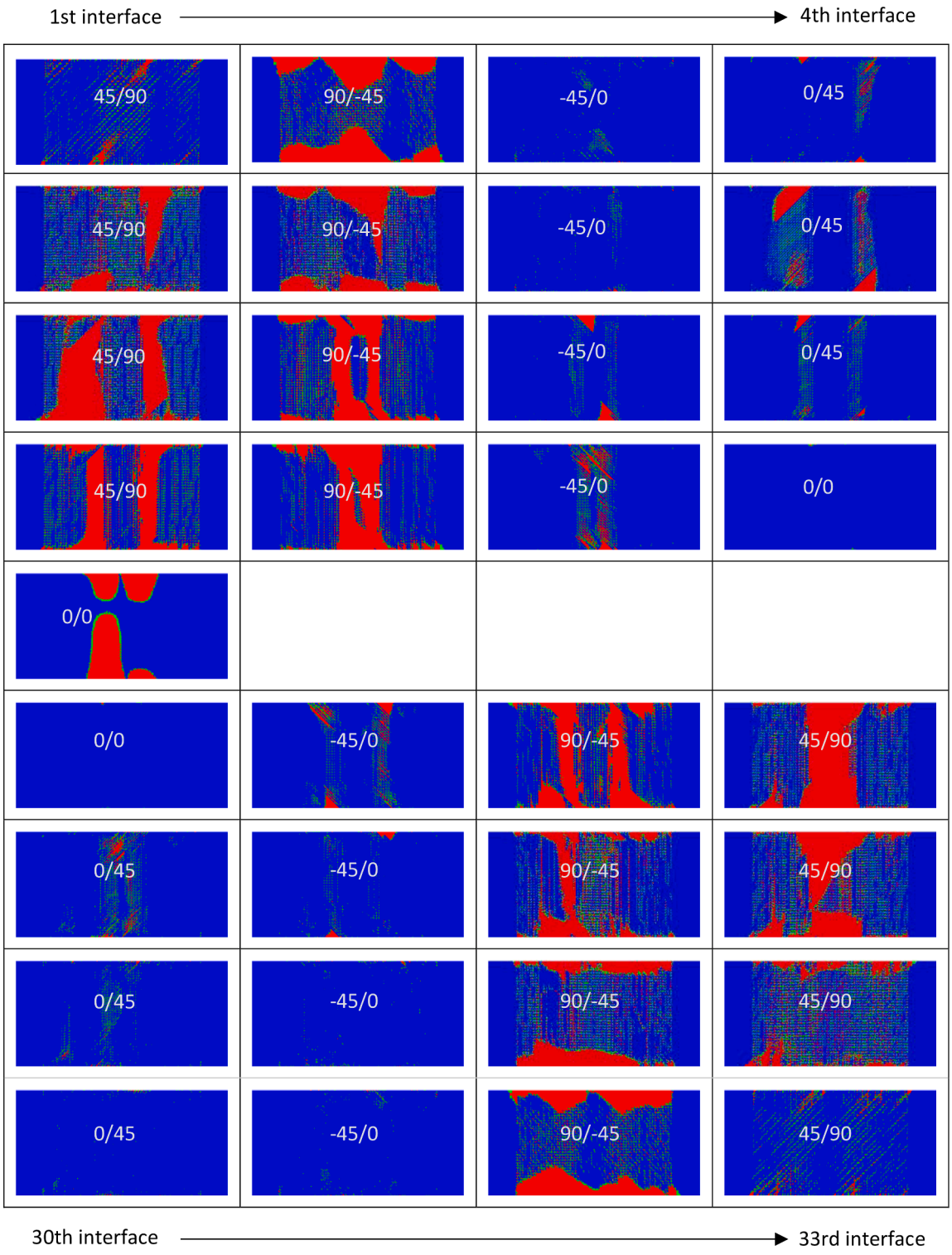

Fig. 20. Predicted interlaminar failure for the wrinkle 50% severity case at 50,000 cycles (red: full failure; green: damaged; blue: elastic).

4.2.3. Wrinkle

Fig. 19 shows that, for all fatigue severities in the wrinkle case, the stiffness slowly decreased with the number of cycles, then suffered a suddenly significant reduction. This more rapid degradation was caused by faster delamination growth in the wrinkle region. Similar to the pristine case as observed in Fig. 15, the wrinkle specimens were also primarily affected by delamination in the 90°/±45° interfaces, as shown by the model in Fig. 20. However, different from the pristine case, the 90°/±45° interfaces in the wrinkle case showed more severe damage in the centre wrinkled region, instead of near the laminate surface; this is particularly true for the 90°/45° interfaces. This was also observed in experiments (Fig. 21). The wrinkle caused a through-thickness shear stress localisation at the wavy plies, which was the driving factor for delamination. FE predictions agree well with experimental measurement in the two low severities, as shown in Fig. 19. The underestimate in the highest severity (60 %) is likely to be a consequence of the extent of bulk damage, i.e. matrix degradation within plies. The bulk damage is underestimated in the simulations, since the solid elements used to

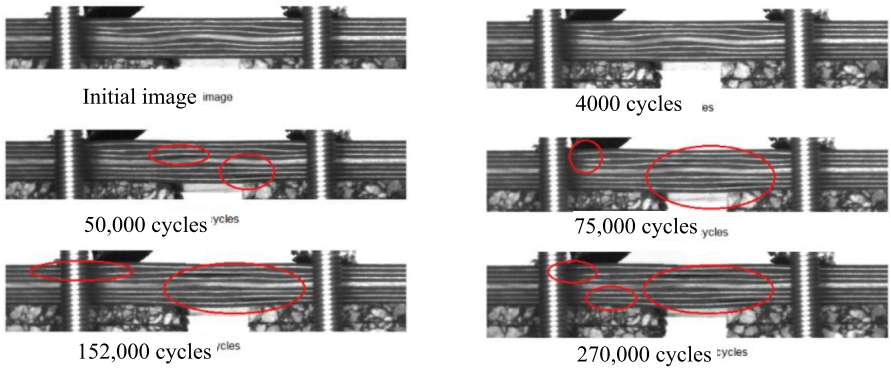

Fig. 21. Camera images showing delamination growth (highlighted in red circles) at various stages of an IM7/8552 wrinkle specimen loaded at 50% fatigue severity.

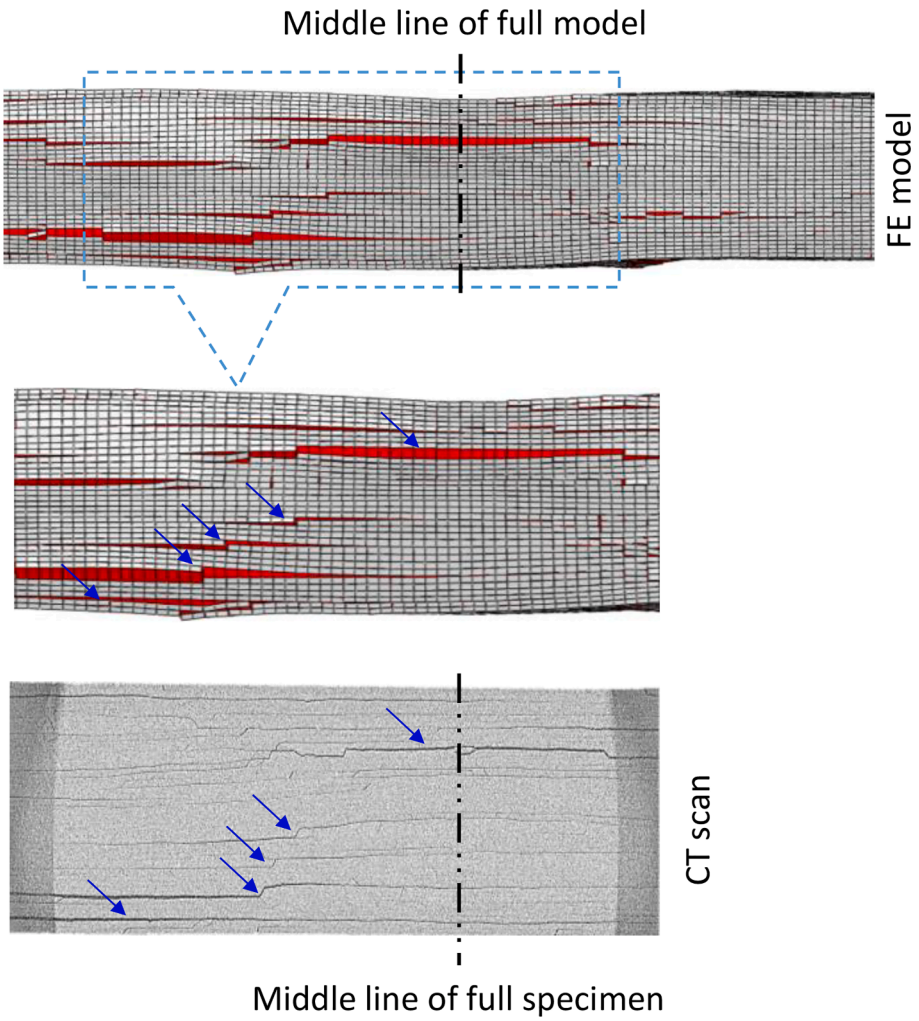

Fig. 22. Side views of the wrinkle 60% severity model and the wrinkle 60% severity specimen No. 2 after fatigue.

model plies, which contain inserted intralaminar cohesive elements as shown in Fig. 3, were assumed to be purely elastic and not subject to fatigue degradation. However, as the number of cycles increases, the model E-N curve shows a trend closer to the experimental curves. Fig. 22 compares side views of the numerical model and a specimen that was tested in the 60 % case. Consistent failure patterns were observed between the two.

4.2.4. *Wrinkle & cut-ply*

Fig. 23 shows the stiffness degradation as a function of elapsed cycles for W&C specimens. The fluctuations present in the wrinkle & cut-ply case are due to more extensive energy released at the beginning of fatigue degradation compared to the winkle only case and the cut-ply only case. As the fatigue degradation stabilised, the fluctuations reduced. FE predictions agree well with experimental measurement of stiffness degradation for all three severities. The stiffness initially decreased gradually with the number of cycles, primarily due to delamination

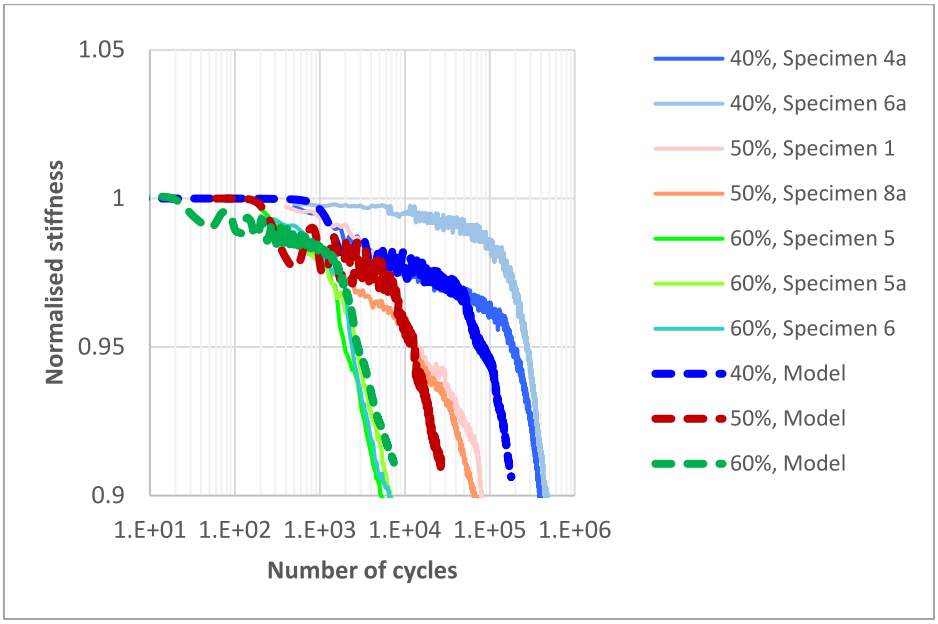

Fig. 23. Experimental measurements and model predictions regarding the normalised stiffness versus number of cycles of the "wrinkle & cut ply" laminates.

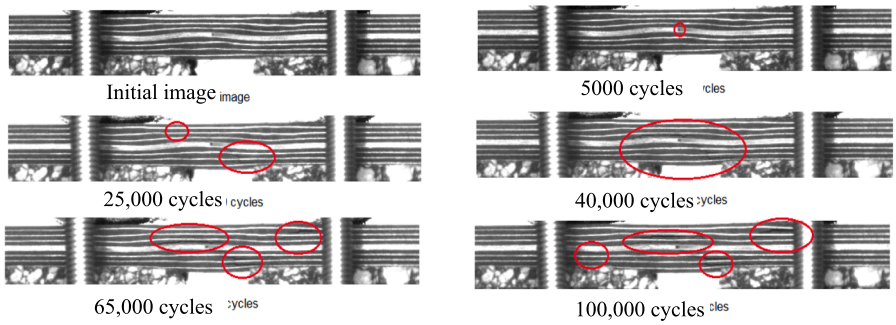

Fig. 24. Camera images showing delamination growth (highlighted in red circles) at various stages of an IM7/8552 W&C specimen loaded at 50 % fatigue severity.

emanating from the cut-ply and propagating along the interfaces between the two central cut 0° plies and their adjacent continuous 0° plies, as observed in Fig. 24 and Fig. 25. The stiffness degradation then became more rapid, primarily because that both the 90°/±45° interface in the major wrinkle region and the two 0°/0° interfaces bounding the cut-ply experienced accelerated delamination growth.

4.2.5. S-N curves

Fig. 26 shows the S-N curves for all cases, based on their respective ultimate strengths or delamination strength (for cut-ply case) and a 5 % stiffness drop. The FE results match the experimental measurements, within a maximum difference of one-decade in terms of elapsed cycles. The underestimate of fatigue life at the highest severity for the wrinkle case is again primarily attributed to the partial description of bulk matrix damage within plies. The experimental pristine 40 % data is not plotted in Fig. 26a, as it did not reach a 5 % stiffness drop at run-out (10^6 cycles), and the FE model gave a conservative estimate to fatigue life in this case.

To compare the effects of these defects/features on the fatigue life, the fatigue severities in the defect cases were re-defined with respect to the ultimate tensile strength of the pristine laminate. The re-plotted S-N curves are compared in Fig. 27. It is very clear that the defects significantly reduce the fatigue life compared to the pristine configuration. This reduction has similar magnitude for the cut-ply feature and the combined wrinkle & cut-ply defect, more pronounced than the wrinkle defect. The relative reduction in strength due to embedded defects is related to the material properties. In this case, the delaminations emanating from defects/features, i.e. cut-ply and wrinkle, dominates. If a material system with a greater resistance to delamination, e.g. a modern interlayer toughened material, were to be tested, the results are likely to be different.

Based on the cases studied here, it is recommended that conservative design guidelines should be adopted for laminates with embedded defects/features subject to cyclic loading. In particular, the design should not be based on allowables derived from quasi-static loading, as these data might be mis-leading with regards to acceptance of composite components containing manufacturing induced defects/features.

4.3. Mesh sensitivity

Cohesive element thickness: The 1×10^{-2} mm thickness gave an apparent decrease in the overall stiffness of the pristine model (global load vs. displacement) compared to 1×10^{-3} mm and 1×10^{-4} mm. The latter two showed negligible difference in the stiffness. 1×10^{-3} mm was used in this study for ease of visualisation, while maintaining the prediction accuracy.

Unit cell size: The modelling results shown in Section 4 were achieved by using the unit cell mesh size of 0.5 mm (recalling Fig. 3a). A mesh sensitivity study was conducted using the pristine 50 % case and the wrinkle 50 % case by varying the unit cell size from 0.5 mm to 1.5

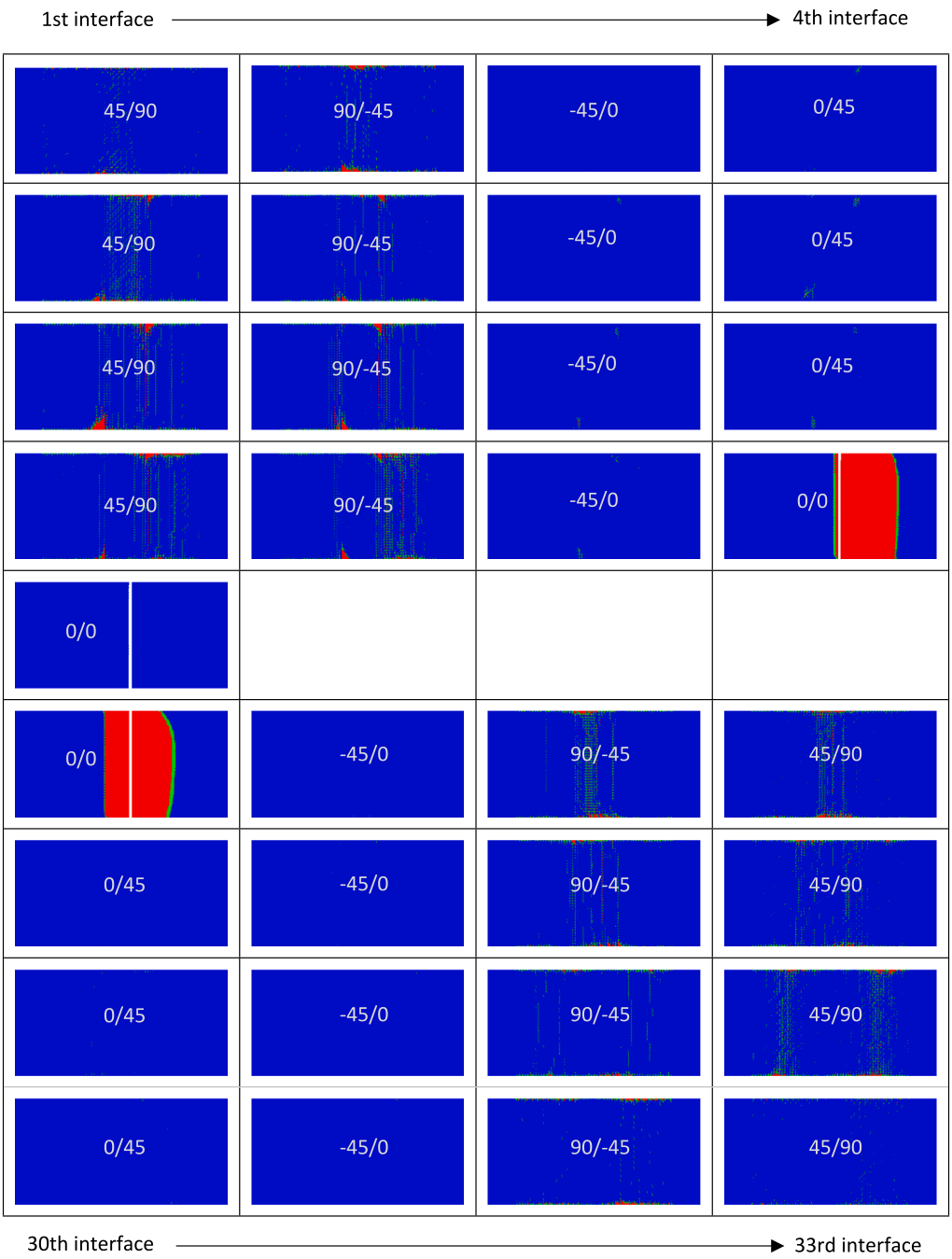

Fig. 25. Predicted interlaminar failure for the W&C 50% severity case at 12,000 cycles (red: full failure; green: damaged; blue: elastic).

mm. As shown in Fig. 28, the results started converging at 1 mm and were converged at 0.5 mm. This agrees well with Ref. [10], where results were well converged at 1 mm.

Fine-mesh length: To save computational cost, the central fine mesh length used for achieving the above results was 30 mm (recall Fig. 4). A mesh sensitivity study was run regarding the fine mesh length using the pristine 50 % case and the wrinkle 50 % case, while the total model length was kept at 90 mm. As shown in Fig. 29, there is negligible difference between 30 mm fine mesh length and 60 mm fine mesh length up to 5 % stiffness knock-down. Beyond 5 % stiffness knock-down, the shorter fine mesh gave an overestimate of the stiffness compared to the longer fine mesh. This is because the coarse mesh region on either side of the fine mesh region artificially suppressed the crack propagation. Thus, the 5 % stiffness knock-down was used to plot S-N curves in Fig. 26 and Fig. 27.

5. Conclusions

This paper investigated the influence of fibre waviness defects and their interaction with ply terminations. The effect of each defect/feature on the strength and fatigue life of a carbon FRP composite laminate was evaluated separately, through an extensive experimental programme and an advanced explicit finite element modelling strategy. The cases considered were out-of-plane wrinkle, cut-ply, and combined wrinkle/cut-ply, embedded in quasi–isotropic IM7/8552 laminates. In-house manufacturing methods were used to introduce the defects and features in coupons. A NI/LabVIEW® program was written to control the loading and collect data from measurement instruments, including capture of specimens at a prescribed rate. Progressive damage FE models were built following a ply-by-ply strategy, where an image-based algorithm was used to replicate the wrinkle defect in the models. Thin

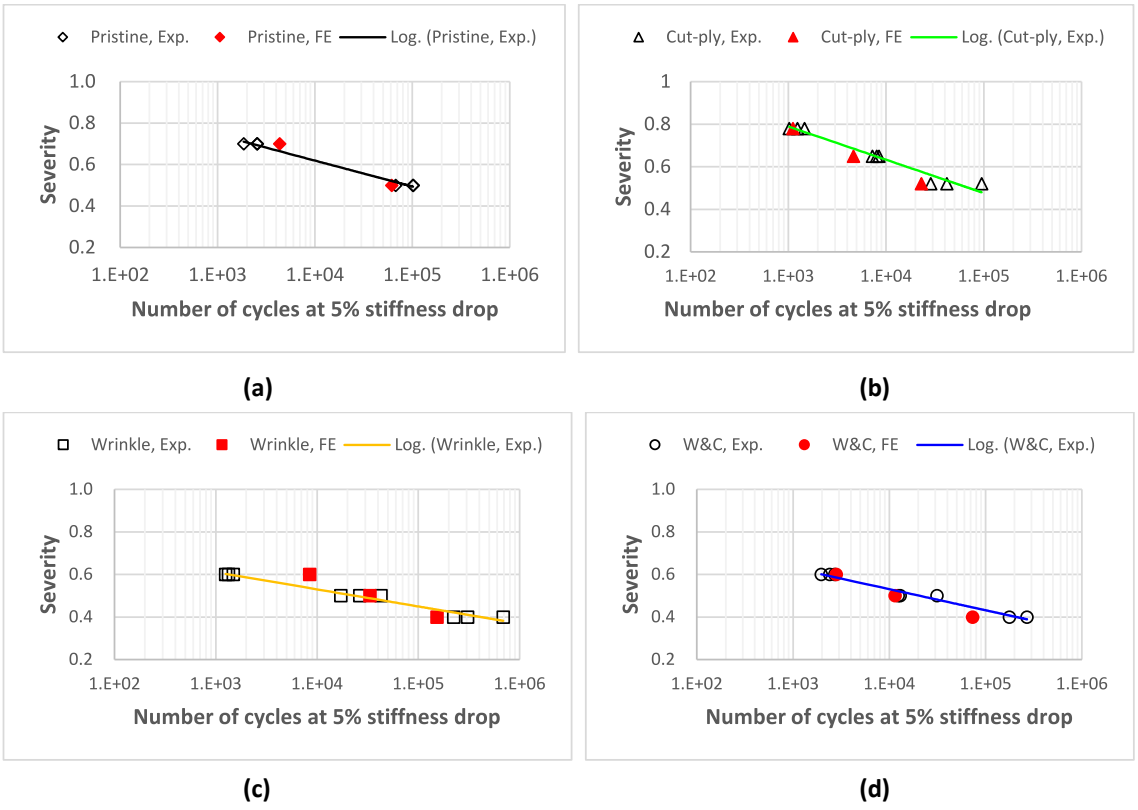

Fig. 26. Severity vs. number of cycles at 5% stiffness knock-down (S-N) curves; (a) pristine, (b) cut-ply, (c) wrinkle and (d) combined wrinkle & cut-ply; note that the cut-ply severities based on delamination strength.

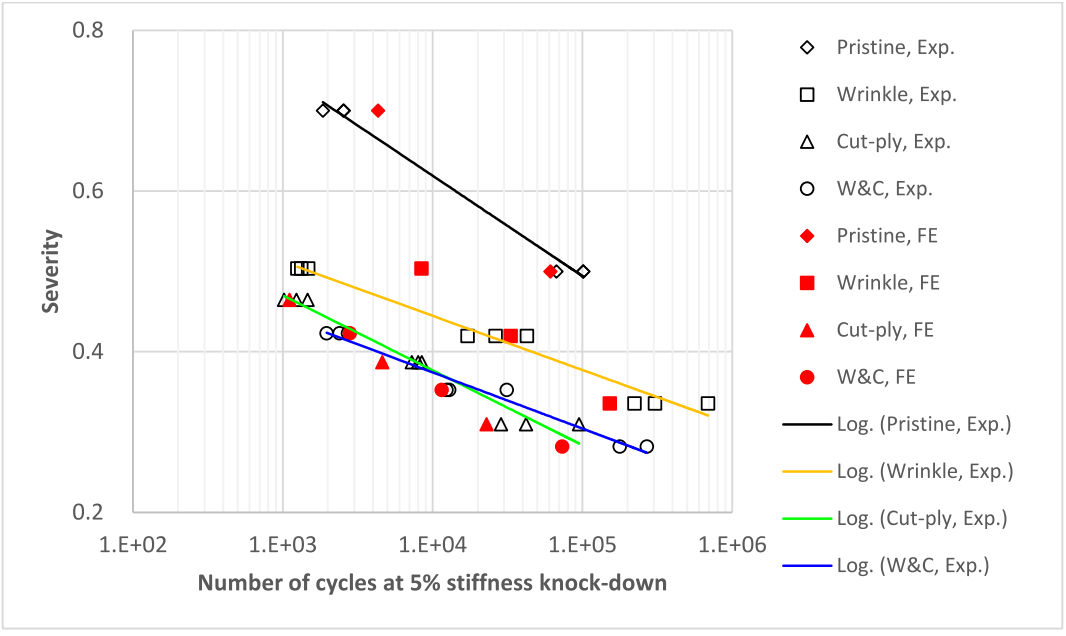

Fig. 27. Severity (based on respective peak stress divided by pristine ultimate static strength) vs. number of cycles to 5% stiffness knock-down (S-N) curves.

cohesive elements were inserted between plies and within plies to predict interlaminar delamination and intralaminar matrix cracking, using an advanced combined static and fatigue formulation developed based on a bi-linear mixed-mode cohesive law.

The presence of the defects/features leads to varying degrees of reduction of ultimate strength for the FRP laminate compared to the pristine case. These respectively are 16.1 % for the wrinkle case, 22.6 % for the cut-ply case and 29.5 % for the W&C case. In all cases, final failure occurred because of extensive fibre failure. The through-width cut-ply primarily caused delamination in the FRP laminate, significantly reducing its load-carrying capability. Thus, a clear load drop was observed in the cut-ply and W&C static test cases. The delamination strength in both cases were around 40 % lower than the ultimate strength of the pristine case. Both the experimental testing and

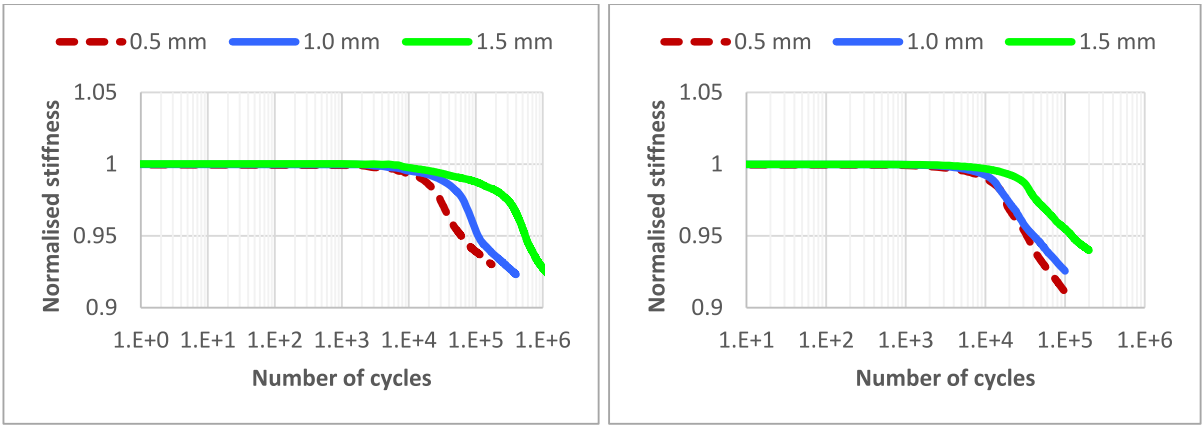

Fig. 28. Model results of (a) the pristine 50% case and (b) the wrinkle 50% case at different unit cell mesh sizes.

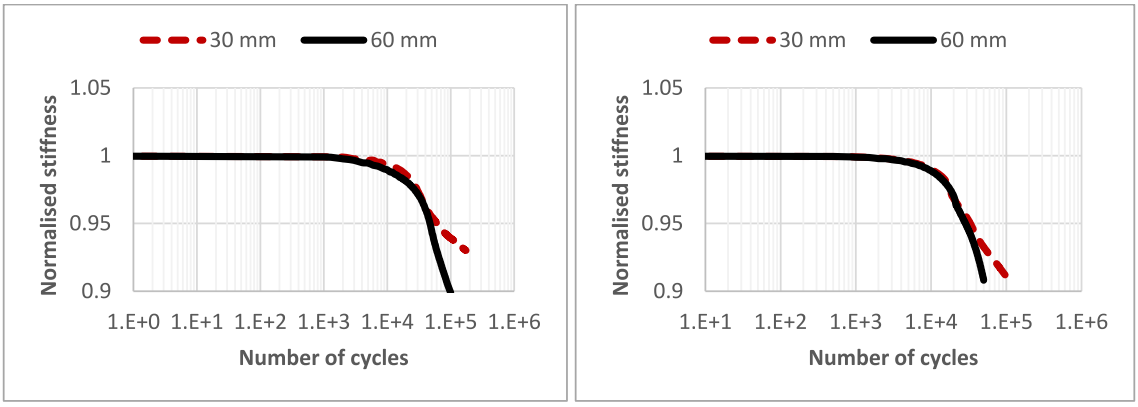

Fig. 29. Model results of (a) the pristine 50% case and (b) the wrinkle 50% case at different fine mesh lengths.

numerical modelling demonstrate good agreement regarding the static ultimate strength in all the cases, as well as for the delamination strength in the cut-ply and W&C cases.

The fatigue life was significantly reduced by the presence of defects and features, being up to two decades shorter at the loading level corresponding to half of the pristine laminate strength. The cut-ply feature and the combined wrinkle plus cut ply have a similar impact on the fatigue life of the laminate, indicating that the ply termination feature dominates the behaviour, and it can be considered more severe than wrinkle. The numerical models provide a good prediction of the fatigue life, both with and without defects/features, with a difference of no more than one decade in terms of number of cycles required for a 5 % stiffness reduction. Detailed failure mechanisms in all the cases have been examined via experimental observations and numerical modelling. In the pristine case, delamination mainly occurred at the interfaces between 90° and −45° plies, while the presence of the wrinkle defect also triggers interlaminar cracking in other interfaces. The ply cut feature results in major delamination originating from the termination itself.

These observations are material and defect-severity specific. Nonetheless, the successful demonstration of the advanced fatigue modelling capability now gives confidence for the use of virtual allowables to account for the knock-down in performance of defects and features (and their combinations) in fibre-reinforced laminates. The key advantage of the proposed modelling approach is that simulations can be employed to predict performance knock-downs for a much wider range of defects and features (and combinations thereof) than those that can be experimentally characterised, with only the most critical for a structure's integrity requiring full validation.

CRediT authorship contribution statement

Bing Zhang: Writing – review & editing, Writing – original draft, Validation, Methodology, Investigation, Formal analysis, Conceptualization. **Hafiz Ali:** Validation, Methodology, Investigation. **Giuliano Allegri:** Writing – review & editing, Validation, Supervision, Methodology, Investigation, Funding acquisition, Formal analysis, Conceptualization. **Stephen R. Hallett:** Writing – review & editing, Validation, Supervision, Resources, Project administration, Methodology, Investigation, Funding acquisition, Data curation, Conceptualization.

Declaration of competing interest

The authors declare that they have no known competing financial interests or personal relationships that could have appeared to influence the work reported in this paper.

Acknowledgements

The authors would like to acknowledge Rolls-Royce plc for the support of this research through the Composites University Technology Centre (UTC) at the University of Bristol, UK. The authors are grateful to Innovate UK for the funding of the Aerospace Technology Institute (ATI) projects "CTI Composite Fan Technology" (Ref. 113085) and FANTASTICAL ("FAN Testing And STatistical Integrity CALibration|, Ref. 113190). Prof Giuliano Allegri would like to acknowledge the support of Innovate UK via the project D-STANDART ("Durability Modelling of Composite Structures with Arbitrary Lay-up using Standardised Testing and Artificial Intelligence", Ref. 10063968) and of the

Royal Academy of Engineering, through his Senior Research Fellowship "Physically Based Modelling of Fatigue in Composites". The authors also wish to thank Mr Mike Jones for help on experiment set-up, Dr Supratik Mukhopadhyay for the discussion on modelling, and Dr Christopher Jones for conducting the CT scan of the fatigue coupons.

Data availability

The authors do not have permission to share data.

References

[1] Chevalier PL, Kassapoglou C, Gürdal Z. Fatigue behavior of composite laminates with automated fiber placement induced defects- a review. Int J Fatigue 2020;140:105775. https://doi.org/10.1016/j.ijfatigue.2020.105775.
[2] Kulkarni P, Mali KD, Singh S. An overview of the formation of fibre waviness and its effect on the mechanical performance of fibre reinforced polymer composites. Compos Part A Appl Sci Manuf 2020;137:106013. https://doi.org/10.1016/j.compositesa.2020.106013.
[3] Belnoue J-P-H, Nixon-Pearson OJ, Thompson AJ, Ivanov DS, Potter KD, Hallett SR. Consolidation-driven defect generation in thick composite parts. J Manuf Sci Eng 2018;140:071006. https://doi.org/10.1115/1.4039555.
[4] Wisnom M, Jones M, Cui W. Delamination in composites with terminating internal plies under tension fatigue loading. Compos Mater Fatigue Fract Fifth 1995:486. https://doi.org/10.1520/STP14031S.
[5] Maragoni L, Carraro PA, Peron M, Quaresimin M. Fatigue behaviour of glass/epoxy laminates in the presence of voids. Int J Fatigue 2017;95:18–28. https://doi.org/10.1016/j.ijfatigue.2016.10.004.
[6] Eliasson S, Hultgren G, Barsoum Z, Wennhage P. Probabilistic fatigue strength assessment of cross-ply laminates: exploring effects of manufacturing defects through a two-scale modeling approach. Compos Struct 2024;330:117844. https://doi.org/10.1016/j.compstruct.2023.117844.
[7] Hörrmann S, Adumitroaie A, Viechtbauer C, Schagerl M. The effect of fiber waviness on the fatigue life of CFRP materials. Int J Fatigue 2016;90:139–47. https://doi.org/10.1016/j.ijfatigue.2016.04.029.
[8] Adams DO. Effects of layer waviness on compression-loaded thermoplastic composite laminates. Virginia Polytechnic Institute and State University; 1991.
[9] Mendonça HG, Mikkelsen LP, Zhang B, Allegri G, Hallett SR. Fatigue delaminations in composites for wind turbine blades with artificial wrinkle defects. Int J Fatigue 2023;175:107822. https://doi.org/10.1016/j.ijfatigue.2023.107822.
[10] Mukhopadhyay S, Nixon-Pearson OJ, Hallett SR. An experimental and numerical study on fatigue damage development in laminates containing embedded wrinkle defects. Int J Fatigue 2018;107:1–12. https://doi.org/10.1016/j.ijfatigue.2017.10.008.
[11] Wang J, Potter KD, Etches J. Experimental investigation and characterisation techniques of compressive fatigue failure of composites with fibre waviness at ply drops. Compos Struct 2013;100:398–403. https://doi.org/10.1016/j.compstruct.2013.01.010.
[12] Miao X, Chen C, Fæster S, Samareh-mousavi SS, Chen X. Fatigue and post-fatigue static crack characterisation of a wrinkled thick glass fibre laminate in a composite wind turbine blade. Int J Fatigue 2023;176.
[13] Miao X, Chen X, Rasmussen S, Mcgugan M. Compression-compression fatigue damage of wrinkled carbon/glass hybrid composite laminates. Compos Struct 2024;346. https://doi.org/10.1016/j.compstruct.2024.118443.
[14] Spencer M, Chen X. Static and fatigue cracking of thick carbon/glass hybrid composite laminates with complex wrinkle defects. Int J Fatigue 2023;177:107963. https://doi.org/10.1016/j.ijfatigue.2023.107963.
[15] Elsherbini YM, Hoa SV. Fatigue threshold-stress determination in AFP laminates containing gaps using IR thermography. Compos Sci Technol 2017;146:49–58. https://doi.org/10.1016/j.compscitech.2017.04.006.
[16] Allegri G, Jones MI, Wisnom MR, Hallett SR. A new semi-empirical model for stress ratio effect on mode II fatigue delamination growth. Compos Part A Appl Sci Manuf 2011;42:733–40. https://doi.org/10.1016/j.compositesa.2011.02.013.
[17] Nikishkov Y, Makeev A, Seon G. Progressive fatigue damage simulation method for composites. Int J Fatigue 2013;48:266–79. https://doi.org/10.1016/j.ijfatigue.2012.11.005.
[18] Elsherbini YM, Hoa SV. Experimental and numerical investigation of the effect of gaps on fatigue behavior of unidirectional carbon/epoxy automated fiber placement laminates. J Compos Mater 2017;51:759–72. https://doi.org/10.1177/0021998316655393.
[19] Shokrieh MM. Progressive fatigue damage modeling of composite materials. McGill University; 1996.
[20] Chen X, Semenov S, McGugan M, Hjelm Madsen S, Cem Yeniceli S, Berring P, et al. Fatigue testing of a 14.3 m composite blade embedded with artificial defects – Damage growth and structural health monitoring. Compos Part A Appl Sci Manuf 2021;140:106189. https://doi.org/10.1016/j.compositesa.2020.106189.
[21] Noh H, Go M-S, Kim JH, Choi Y-H, Kim J-G. Numerical modeling and experimental validation of lamina fracture and progressive delamination in composite dovetail specimens under tensile loading. Compos Struct 2023;325:117578. https://doi.org/10.1016/j.compstruct.2023.117578.
[22] Vassilopoulos AP. The history of fiber-reinforced polymer composite laminate fatigue. Int J Fatigue 2020;134:105512. https://doi.org/10.1016/j.ijfatigue.2020.105512.
[23] Ferdous W, Manalo A, Peauril J, Salih C, Raghava Reddy K, Yu P, et al. Testing and modelling the fatigue behaviour of GFRP composites – Effect of stress level, stress concentration and frequency. Eng Sci Technol an Int J 2020;23:1223–32. https://doi.org/10.1016/j.jestch.2020.01.001.
[24] Ansari MTAA, Singh KK, Azam MS. Fatigue damage analysis of fiber-reinforced polymer composites — A review. J Reinf Plast Compos 2018;37:636–54. https://doi.org/10.1177/0731684418754713.
[25] Hallett SR, Green BG, Jiang WG, Wisnom MR. An experimental and numerical investigation into the damage mechanisms in notched composites. Compos Part A Appl Sci Manuf 2009;40:613–24. https://doi.org/10.1016/j.compositesa.2009.02.021.
[26] Tao C, Mukhopadhyay S, Zhang B, Kawashita LF, Qiu J, Hallett SR. An improved delamination fatigue cohesive interface model for complex three-dimensional multi-interface cases. Compos Part A Appl Sci Manuf 2018;107:633–46. https://doi.org/10.1016/j.compositesa.2018.02.008.
[27] Zhang B, Kawashita LF, Hallett SR. Composites fatigue delamination prediction using double load envelopes and twin cohesive models. Compos Part A Appl Sci Manuf 2020;129:105711. https://doi.org/10.1016/j.compositesa.2019.105711.
[28] Zhang B, Kawashita LF, Jones MI, Lander JK, Hallett SR. An experimental and numerical investigation into damage mechanisms in tapered laminates under tensile loading. Compos Part A Appl Sci Manuf 2020;133:105862. https://doi.org/10.1016/j.compositesa.2020.105862.
[29] Robinson P, Galvanetto U, Tumino D, Bellucci G, Violeau D. Numerical simulation of fatigue-driven delamination using interface elements. Int J Numer Methods Eng 2005;63:1824–48. https://doi.org/10.1002/nme.1338.
[30] Harper PW, Hallett SR. A fatigue degradation law for cohesive interface elements - Development and application to composite materials. Int J Fatigue 2010;32:1774–87. https://doi.org/10.1016/j.ijfatigue.2010.04.006.
[31] Turon A, Costa J, Camanho PP, Dávila CG. Simulation of delamination in composites under high-cycle fatigue. Compos Part A Appl Sci Manuf 2007;38:2270–82. https://doi.org/10.1016/j.compositesa.2006.11.009.
[32] Kawashita LF, Hallett SR. A crack tip tracking algorithm for cohesive interface element analysis of fatigue delamination propagation in composite materials. Int J Solids Struct 2012;49:2898–913. https://doi.org/10.1016/j.ijsolstr.2012.03.034.
[33] Bak BLV, Turon A, Lindgaard E, Lund E. A benchmark study of simulation methods for high-cycle fatigue-driven delamination based on cohesive zone models. Compos Struct 2017;164:198–206. https://doi.org/10.1016/j.compstruct.2016.11.081.
[34] Carreras L, Turon A, Bak BLV, Lindgaard E, Renart J, Martin de la Escalera F, et al. A simulation method for fatigue-driven delamination in layered structures involving non-negligible fracture process zones and arbitrarily shaped crack fronts. Compos Part A Appl Sci Manuf 2019;122:107–19. https://doi.org/10.1016/j.compositesa.2019.04.026.
[35] de Moura MFSF, Gonçalves JPM. Cohesive zone model for high-cycle fatigue of adhesively bonded joints under mode I loading. Int J Solids Struct 2014;51:1123–31. https://doi.org/10.1016/j.ijsolstr.2013.12.009.
[36] Iarve EV, Hoos K, Braginsky M, Zhou E, Mollenhauer DH. Progressive failure simulation in laminated composites under fatigue loading by using discrete damage modeling. J Compos Mater 2017;51:2143–61. https://doi.org/10.1177/0021998316681831.
[37] Pirondi A, Moroni F. Improvement of a cohesive zone model for fatigue delamination rate simulation. Materials (Basel) 2019;12:181. https://doi.org/10.3390/ma12010181.
[38] Dávila CG. From S-N to the Paris law with a new mixed-mode cohesive fatigue model for delamination in composites. Theor Appl Fract Mech 2020;106:102499. https://doi.org/10.1016/j.tafmec.2020.102499.
[39] Bak BLV, Turon A, Lindgaard E, Lund E. A simulation method for high-cycle fatigue-driven delamination using a cohesive zone model. Int J Numer Methods Eng 2016;106:163–91. https://doi.org/10.1002/nme.5117.
[40] Jiang W-G, Hallett SR, Green BG, Wisnom MR. A concise interface constitutive law for analysis of delamination and splitting in composite materials and its application to scaled notched tensile specimens. Int J Numer Methods Eng 2007;69:1982–95. https://doi.org/10.1002/nme.1842.
[41] Gan KW, Hallett SR, Wisnom MR. Measurement and modelling of interlaminar shear strength enhancement under moderate through-thickness compression. Compos Part A Appl Sci Manuf 2013;49:18–25. https://doi.org/10.1016/j.compositesa.2013.02.004.
[42] Li X, Hallett SR, Wisnom MR. Predicting the effect of through-thickness compressive stress on delamination using interface elements. Compos Part A Appl Sci Manuf 2008;39:218–30. https://doi.org/10.1016/j.compositesa.2007.11.005.
[43] May M, Hallett SR. A combined model for initiation and propagation of damage under fatigue loading for cohesive interface elements. Compos Part A Appl Sci Manuf 2010;41:1787–96. https://doi.org/10.1016/j.compositesa.2010.08.015.
[44] May M, Hallett SR. An assessment of through-thickness shear tests for initiation of fatigue failure. Compos Part A Appl Sci Manuf 2010;41:1570–8. https://doi.org/10.1016/j.compositesa.2010.07.005.
[45] Allegri G, Wisnom MR, Hallett SR. A new semi-empirical law for variable stress-ratio and mixed-mode fatigue delamination growth. Compos Part A Appl Sci Manuf 2013;48:192–200. https://doi.org/10.1016/j.compositesa.2013.01.018.
[46] Zhang B, Allegri G, Hallett SR. Embedding artificial neural networks into twin cohesive zone models for composites fatigue delamination prediction under

various stress ratios and mode mixities. Int J Solids Struct 2022;236–237:111311. https://doi.org/10.1016/j.ijsolstr.2021.111311.
[47] Raimondo A, Bisagni C. Analysis of local stress ratio for delamination in composites under fatigue loads. AIAA J 2020;58:455–63. https://doi.org/10.2514/1.J058465.
[48] Harper PW, Hallett SR. Cohesive zone length in numerical simulations of composite delamination. Eng Fract Mech 2008;75:4774–92. https://doi.org/10.1016/j.engfracmech.2008.06.004.